PHYSIK-DEPARTMENT

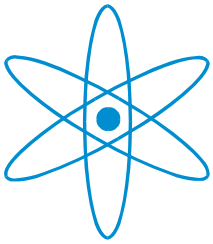

The Kondo exciton: non-equilibrium dynamics after a quantum quench in the Anderson impurity model

Diplomarbeit
von

Markus Johannes Hanl

TECHNISCHE UNIVERSITÄT
MÜNCHEN

Contents

Abstract

The absorption of a photon by a semiconductor quantum dot (QD) can be considered as a quantum quench, where a previously empty energy level in the QD gets suddenly occupied. In this thesis the non-equilibrium dynamics are examined that follow such a quantum quench. The studies consider mainly the absorption lineshape and the time-evolution of spin and charge. Various quantities influencing the lineshape are shortly discussed, too. The absorption spectrum can be divided in three frequency regimes, corresponding to the three fixed points of the single-impurity Anderson Hamiltonian. The three frequency regimes of the absorption lineshape are described both numerically and analytically, where special emphasis is put on the small detuning regime of the lineshape, which corresponds to an excitonic Kondo state in the dot. For such small frequencies, the lineshape behaves according to a power-law and diverges for very small detuning close to the threshold frequency, below which absorption abruptly ceases, resulting in a highly asymmetric lineshape. It is shown that the exponent of the power law divergence can be tuned by magnetic field and can even take on opposite signs for different polarization of the incident photon, which changes the shape of the absorption lineshape completely. The temperature-dependence of the lineshape is also studied. At temperatures smaller than the Kondo temperature T_K, the lineshape is smeared out for frequencies with energy lower than k_BT. If temperature lies above T_K, the peak-width of the absorption spectrum is given by the Korringa relaxation rate which is significantly smaller than the frequency corresponding to k_BT.

Chapter 1

Introduction

Quantum dots (QD) are artificial objects with an extent somewhere between the nano- or the lower micrometer-scale, which can contain one up to several thousand electrons. They are often referred to as artificial atoms, since they possess a system of discrete energy levels, like atoms, and their size and shape can be defined artificially with means of nanofabrication technology. The interaction between the quantum dot and its environment can be described as a system of discrete energy levels coupled to a reservoir of electrons via tunneling-processes [1].

Due to the coupling between dot and reservoir, and the presence of interactions on the dot, electron correlations can arise. In dots that contain only a few electrons and at which the topmost discrete energy level below the Fermi-level of the reservoir contains only a single electron, below a characteristic crossover temperature T_K (the Kondo Temperature) the Kondo Effect can occur [2], a many-body effect that screens the local magnetic moment of the QD into a spin singlet by building up strong spin correlations between the dot spin and the spins of the reservoir electrons. The Kondo effect per se was discovered in the 1930's as resistivity measurements of dilute magnetic alloys showed unexpected results: as the metal is cooled down, resistivity increases again below a certain temperature [3]. 30 years later J. Kondo explained this increase of resistivity with the existence of magnetic impurities in the metal that enable scattering of the electrons at their magnetic moments [2]. His calculation, which was perturbative in the spin exchange coupling, yielded a diverging resistivity for very low temperatures and could not be applied to the latter temperature regime. This was done by K. G. Wilson [4] who developed a non-perturbative method in 1974 and 1975, the numerical renormalization group (NRG), and finally presented a solution to this long-standing problem.

During the decades over which the theory of the Kondo effect was developed, experimentalists turned their interest to other physical problems. Due to the rapid development of nanofabrication technology over the last years, however, the Kondo effect again has enjoyed much attention from the experimental side. With quantum dots it became possible to examine the Kondo effect in an artificial environment [5], [6], [7], to confirm theoretical predictions [8] and even to tune the parameters of the Kondo effect [9] as desired. So far, most experiments studying the Kondo effect were transport measurements. With optical methods the Kondo effect has not been detected yet, though experiments pointing in this direction have been performed

[10], [11]. Theoretical work [12], [13] concerned with optics and the Kondo effect, mostly involved analytical methods.

Tying in with this work, the main goal of this thesis is to examine the optical properties of a QD, which is coupled to a fermionic reservoir and exhibits Kondo physics, by studying its absorption spectrum. Since the absorption of a photon by a QD can be considered as a quantum quench, this study is complemented by the examination of the non-equilibrium dynamics following such a quantum quench; thereby giving insight into arguably the most extensively studied many-body problem, a quantum impurity described by the Anderson model, and, closely related to it, the Kondo effect. We calculate these quantities using a method that had enough power to give a consistent explanation of the Kondo effect for the first time: the NRG-method.

In chapter 2 (model) several different models that are relevant for this thesis are discussed. Apart from the Excitonic Anderson model on which the calculations of this thesis are based, and the Anderson model which is the underlying basis model, the Kondo model is also briefly introduced. Further, the Anderson model is used to illustrate the Kondo effect.

Chapter 3 (experimental background) summarizes the experimental work foregoing this thesis. The ultimative aim is to observe the Kondo effect with optical methods. Although this has not been achieved so far, there have been experiments that give hints that this aim is not far away and how it could be accomplished.

Chapter 4 (calculations) gives a detailed description of how the calculations for this thesis were done. First, the NRG-method is introduced, in the improved form in which it is used today, where complete basis sets can be obtained. Moreover, the numerical calculations of the most interesting quantities will be explained.

The results of the calculations are presented in Chapter 5 (results). The most important part is the discussion of the absorption spectrum. It is shown how the time evolution of charge and spin after photon-absorption is related to the spectrum. Furthermore, the dependence of the absorption lineshape on B-field and temperature is examined and it is pointed out how information about physical quantities describing the system can be obtained from the lineshape.

In Chapter 6 the conclusions are presented and some special details concerning the main part of the thesis are added as appendix.

Chapter 2

Model

2.1 Anderson Model

The Single Impurity Anderson Model (SIAM) describes an impurity in a metal or a single QD by modelling it as an energy level with a local interaction and a hybridization term that enables tunneling to a surrounding Fermi Reservoir (FR).

The Hamiltonian can be divided into three parts

$$H = H_{QD} + H_c + H_t \tag{2.1}$$

where the Hamiltonians on the r. h. s. consist of the following terms:

$$H_{QD} = \sum_{\sigma=\uparrow,\downarrow} \varepsilon_{e\sigma} n_{e\sigma} + U n_{e\uparrow} n_{e\downarrow} \tag{2.2}$$

$$H_c = \sum_{\vec{k}\sigma} \varepsilon_{\vec{k}\sigma} c^\dagger_{\vec{k}\sigma} c_{\vec{k}\sigma} \tag{2.3}$$

$$H_t = \sqrt{\Gamma/\pi\rho} \sum_{\vec{k}\sigma} (e^\dagger_\sigma c_{\vec{k}\sigma} + h.c.) = \sqrt{\Gamma/\pi\rho} \sum_{\sigma} (e^\dagger_\sigma c_\sigma + h.c.) \tag{2.4}$$

with $n_{e\sigma} = e^\dagger_\sigma e_\sigma$, $c_\sigma = \sum_k c_{k\sigma}$

H_{QD} is the Hamiltonian describing the QD. The first term describes the energy of the electrons on the e-level $\varepsilon_{e\sigma}$ with respect to the Fermi Energy, where σ denotes the spin of the electron. The second term accounts for the local Coulomb repulsion on the dot and is only non-zero if the dot is occupied by both electrons, which is probed by the number-operators $n_{e\sigma}$

H_c describes the environment as a reservoir of many non-interacting electrons. Their energies $\varepsilon_{k\sigma}$ are assumed to depend only on the absolute value of k with $-D < \varepsilon_{k\sigma} < +D$, where $2D$ is the bandwidth of the reservoir.

H_t connects the dot and the reservoir by allowing tunneling between e-level and FR. Tunneling processes are determined by the density of states ρ and Γ, of which the latter can be seen as a measure for the coupling strength between dot and

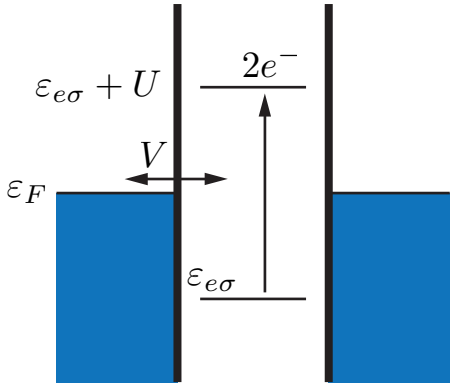

Figure 2.1: Single Impurity Anderson Model. The dot is coupled to a Fermionic reservoir (indicated blue). The local level $\varepsilon_{e\sigma}$ is separated from the reservoir by Coulomb barriers (indicated by thick black lines) through which electrons can tunnel. Tunneling strength is determined by the transition matrix element V. If the local level is occupied by two electrons their energy is increased by U due to Coulomb repulsion

reservoir. The prefactor of the Hamiltonian $\sqrt{\Gamma/\pi\rho}$ is determined by the hybridization matrix element between dot and reservoir $\sqrt{\Gamma/\pi\rho} = \langle\psi_{QD}|H|\psi_c\rangle$ where $\langle\psi_{QD}|$ and $|\psi_c\rangle$ are electron wavefunctions on the dot and in the reservoir, respectively. Coupling does not depend on k, i. e. it is assumed that all states of the reservoir are coupled to the dot with equal strength. For this reason the tunneling Hamiltonian H_t depends only on the combination of operators $c_\sigma = \sum_k c_{k\sigma}$ (see Eq. (2.4)).

The above model was proposed by P. W. Anderson [14] in the 1960s and is widely used to model impurities in metals or Quantum Dots. It can easily be generalized to several local levels and reservoirs, however the problems arising from these models can be very difficult to solve. These general Anderson models are subject of current research, but are not considered in this thesis.

2.2 The Kondo Effect

The Kondo Effect emerges when a localized spin degree of freedom, provided e.g. by a single molecule, a magnetic impurity or an unpaired electron in a quantum dot, is coupled to a continuous reservoir of electrons. The Kondo Effect is a many-body effect where the spin of the localized single electron is totally screened to an effective spin singlet by electrons from the surrounding reservoir. This screening sets in once the temperature T crosses below a characteristic temperature, the Kondo temperature T_K. There are several ways to determine T_K. In this thesis, it was determined according to $\chi_0 = 1/4T_K$ [15], where χ_0 is the magnetic susceptibility

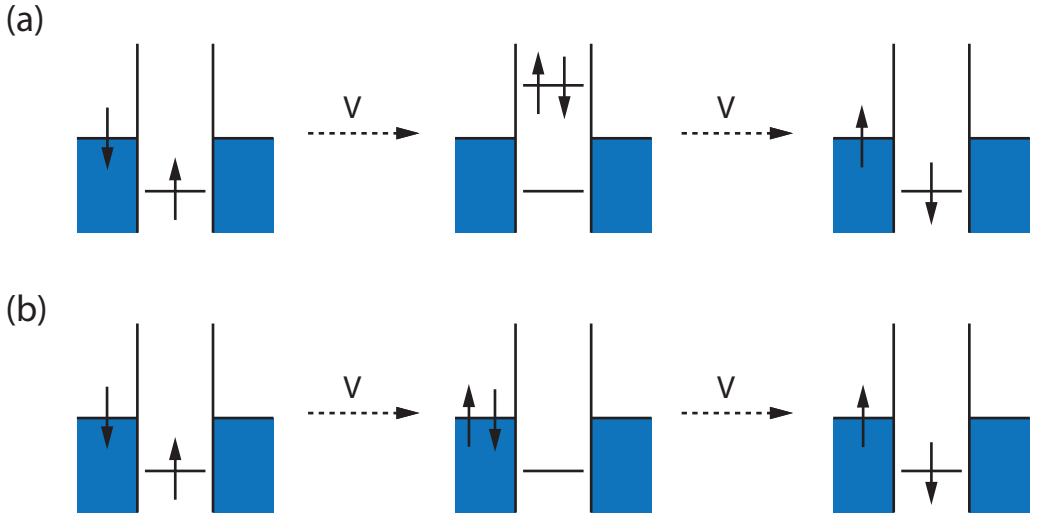

Figure 2.2: Virtual processes that result in a spin-flipped state. (a) An electron tunnels from the reservoir onto the dot into a virtual excited state. The electron that had previously occupied the dot tunnels back and the dot-electron is flipped. (b) An electron from the dot tunnels into the reservoir and an electron with opposite spin tunnels back.

at $T = 0$, which was calculated with NRG. This definition is very convenient for accurate numerical evaluation. In situations in which its use was very unpractical, the formula [16] (see also (2.4))

$$T_K = \sqrt{\Gamma U/2} e^{-\pi|\varepsilon_e(\varepsilon_e+U)|/(2U\Gamma)}, \tag{2.5}$$

was used instead, which gives essentially equivalent results.

The electron on the e-level couples to the FR via tunneling. Through tunneling processes it is possible that a spin flip occurs on the dot; the two lowest-order virtual processes at which the spin is flipped are shown in Fig. 2.2. In Fig. 2.2a an electron tunnels from the reservoir to the dot and an electron from the dot tunnels back. This process requires the energy $(\varepsilon_{e\sigma}) + U$. Since this energy is not freely available, the process must occur at a time scale of $\Delta t \approx \hbar(\varepsilon_{e\sigma} + U)$ at which energy conservation can be violated. If the electron tunneling back to the e-level has different spin than the one tunneling out, the spin of the QD-electron is flipped. In Fig. 2.2b the electron tunnels *from the e-level* into the FR and one electron from the FR tunnels back, the relevant time scale is given by $\Delta t \approx \hbar|\varepsilon_{e\sigma}|$.

At energies below T_K ($k_B = \hbar = \mu_B = 1$ throughout the thesis) the system is in a state where electrons from the reservoir continuously tunnel from the FR onto the local level and back. At these low energy states the spin-flips induced by virtual processes happen so often, that the spin of the local electron gets screened and forms a spin singlet. However this spin-screening is mainly caused by higher order processes, like the one shown in Fig. 2.3 at which the spin-flipped state is an

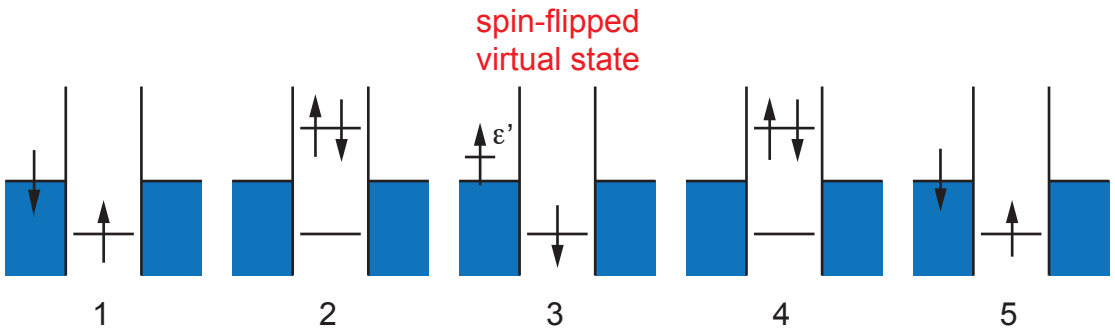

Figure 2.3: Example of a fourth order virtual process that contributes to the spin-screening at a Kondo state. Higher order virtual processes with a virtual spin-flipped intermediate state produce the spin-screening that is typical for the Kondo-regime.

intermediate state of the virtual processes.

Because of this frequent tunneling, which involves a variety of virtual states, the density of states drastically increases around the ground state energy, resulting in the so called Kondo-peak in the local density of states (LDOS). This can be seen in Fig. 2.4 where the local density of states $A(\omega)$ is shown within a schematic figure of the Anderson model. The smaller peaks of the LDOS at the local levels are determined by the hybridization between local level and reservoir and have width Γ.

2.3 Excitonic Anderson Model

To calculate the absorption spectrum, the Excitonic Anderson Model is used, an extension of the Anderson Model (2.1). At an absorption process, an incident photon is absorbed by a semiconductor quantum dot and creates a particle-hole pair. The hole is thereby created in the valence level, which is far below the local level and not connected to the reservoir. Whereas a static quantum dot with a single local level can usually be described by the Anderson Model, this model must now be extended for a proper description of the absorption process, where the extension must contain the energy of the hole, the excitonic Coulomb attraction and the interaction between photon and dot. The new Hamiltonian for the Excitonic Anderson Model (EAM) is then given by:

$$H_{EAM} = H_{QD} + H_c + H_t + H_h + H_{eh} + H_L \tag{2.6}$$

$$H_h = \sum_{\sigma} \varepsilon_{h\sigma} + U_h n_{h\uparrow} n_{h\downarrow} \tag{2.7}$$

$$H_{eh} = -\sum_{\sigma,\sigma'} U_{eh} n_{e\sigma}(1 - n_{h\sigma'}) \tag{2.8}$$

$$H_L = \sum_{k} (\gamma_k \hat{a}_k e_\sigma^\dagger h_{\bar{\sigma}}^\dagger \mathrm{e}^{-i\omega_k t} + h.c.). \tag{2.9}$$

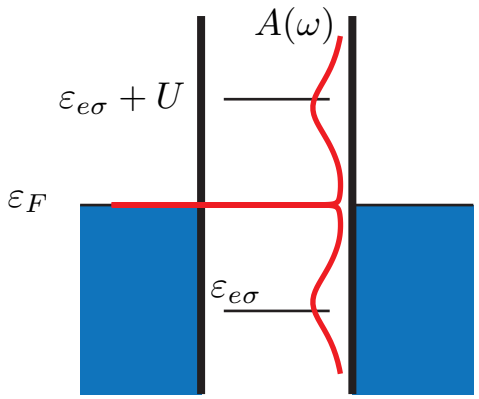

Figure 2.4: Kondo-peak in the local density of states. For $T < T_K$ the variety of possible tunneling processes drastically increases the local density of states $A(\omega)$ (red line) around the Fermi energy. This becomes visible as a sharp resonance in the local density of states. The LDOS also has smaller peaks at the local levels (Hubbard-side-peaks) which have width Γ.

H_h is thereby the Hamiltonian for the valence level where the first term describes the energy of the holes and the second term the Coulomb repulsion of two holes in the valence level. H_{eh} accounts for the Coulomb attraction between electrons in the local level and holes in the valence level. H_L describes the interaction between photon and dot, it creates an electron at the local level and a hole at the valence level, by $e_\sigma^\dagger$ and $h_{\bar{\sigma}}^\dagger$, respectively. $\hat{a}_k$ annihilates a photon with wave vector k and $\gamma_k = \gamma$ is the coupling strength of the photon to the two-level system which will be assumed to be independent of k. Since the quantization of the photon field will not be relevant for the discussions below, H_L can be written as:

$$H_L = \gamma(e_\sigma^\dagger h_{\bar{\sigma}}^\dagger + h.c.). \tag{2.10}$$

In this thesis, only processes are examined where one hole is created in a previously fully occupied valence level. For this special problem, it is simpler to think in terms of two different Hamiltonians, H^i and H^f, one for the initial state before absorption and one for the final state with Coulomb attraction. *Therefore all further discussions will be presented in terms of H^i and H^f.*

The initial and the final Hamiltonian consist of three parts:

$$H^{i/f} = H_{QD}^{i/f} + H_c + H_t \tag{2.11}$$

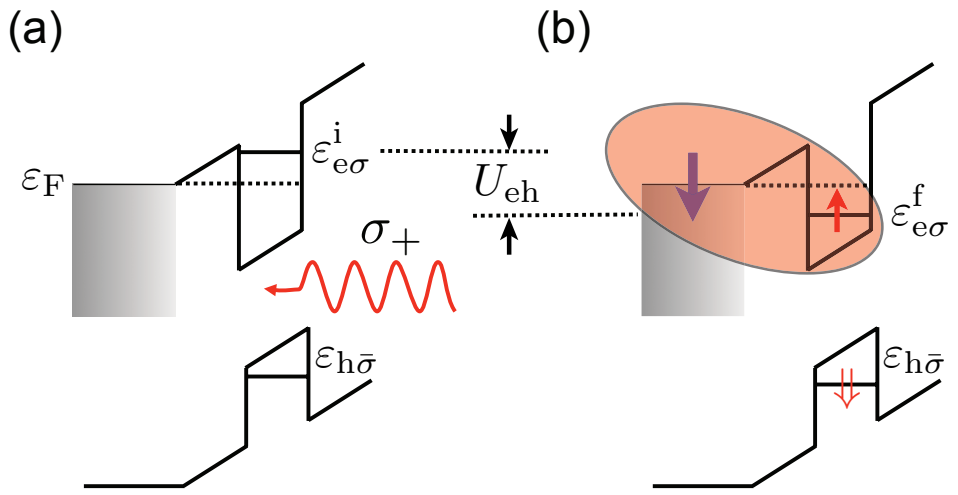

Figure 2.5: Schematic figure the excitonic Anderson model and the corresponding absorption process. Due to photon absorption a hole is created in the valence level which pulls the e-level down by the electron-hole attraction U_{eh}. After absorption the position of the e-level is below the Fermi-level so that the electron is stabilized against flowing away into the FR, but can build out hybridization states.

$$H^a_{QD} = \sum_\sigma \varepsilon^a_{e\sigma} n_{e\sigma} + U n_{e\uparrow} n_{e\downarrow} + \delta_{af}\varepsilon_{h\bar{\sigma}} \qquad (a = i, f) \tag{2.12}$$

$$H_c = \sum_{k\sigma} \varepsilon_{k\sigma} c^\dagger_{k\sigma} c_{k\sigma} \tag{2.13}$$

$$H_t = \sqrt{\Gamma/\pi\rho} \sum_\sigma (e^\dagger_\sigma c_\sigma + h.c.). \tag{2.14}$$

These Hamiltonians are equal to the SIAM-Hamiltonian, however, they differ in (i) the position of their e-levels ($\varepsilon^i_{e\sigma}$ and $\varepsilon^f_{e\sigma} = \varepsilon^i_{e\sigma} - U_{eh}$), where the e-level of the final Hamiltonian is pulled down by the excitonic Coulomb attraction and (ii) in an additional term of $\delta_{af}\varepsilon_{h\bar{\sigma}}$ that accounts for the energy of the hole. Due to the Kronecker-delta, δ_{af}, this term is only "activated" if the system is in its final state (see Fig. 2.5).

If a magnetic field is applied parallel to the growth-direction of the QD, which will be the case at some of the calculations presented later, the local level splits in two separate levels, $\varepsilon_{e\sigma} = \varepsilon_e + \frac{1}{2}\sigma g_e B$, and the energy of the electrons in the FR changes according to $\varepsilon_{k\sigma} = \varepsilon_k + \frac{1}{2}\sigma g_c B$ where g_e and g_c are the g-factors of the electrons on the dot or in the FR, respectively.

2.4 Kondo Model

Although the Kondo model is not used for the examinations described in this thesis, it will briefly be mentioned here. This is justified because as the Anderson Model, this model is widely used to describe impurity problems and is related to

the Anderson Model in many ways. The idea behind the Kondo model is that a single magnetic moment $\vec{S}$ interacts with the accumulated spin of the FR electrons $\vec{s} = \frac{1}{2}\sum_{kk'\sigma\sigma'} c^\dagger_{k\sigma}\vec{\tau}_\sigma\sigma' c_{k\sigma'}$. This causes an effective spin-spin-coupling $\vec{S}\cdot\vec{s}$ and leads to the following Hamiltonian:

$$H_K = 2J\vec{S}\cdot\vec{s} + \sum_{k\sigma}\varepsilon_k c^\dagger_{k\sigma}c_{k\sigma}, \tag{2.15}$$

where the coupling constant J determines the coupling strength. Since the local level interacts with the Fermi-sea only via spin-spin-coupling, this model can describe only spin-, but no charge-fluctuations.

Note that the Kondo model is more "elementary" than the Anderson model. The Kondo effect can be explained in the same way as in (2.2): virtual spin-flipped states screen the local moment. Here however, spin-flips are only possible without charge fluctuations. The Kondo temperature can be determined by the so called poor man's scaling method [17]. Calculations to third order in J yield for the Kondo temperature

$$T_K \sim D_{KM}|2J\rho|^2 e^{-1/2J\rho}, \tag{2.16}$$

where D_{KM} is the effective bandwidth of the Kondo model which is proportional to the Coulomb energy of the Anderson model U.

The Schrieffer-Wolff transformation [18], maps the Single Impurity Anderson model on the Kondo model and yields a relation between J and Γ:

$$J(\Gamma) = -\frac{\Gamma}{\pi\rho}\frac{U}{(U+\varepsilon_{e\sigma})\varepsilon_{e\sigma}}\,. \tag{2.17}$$

The Kondo temperature for the Anderson model (Eq. (2.5)) can then be obtained from Eq. (2.16) and Eq. (2.17).

Chapter 3

Experimental background

3.1 Experimental setup

The model described above can be experimentally realized with self assembled InAs quantum dots. On a GaAs-layer, InAs arranges itself in a monolayer, the so-called wetting layer, with several dots on it. The dots emerge due to the different lattice constants of GaAs and InAs, which makes dots energetically more favorable than a second plain InAs-layer. In the InAs-plane, the dots are then surrounded by the wetting-layer, which acts as electron reservoir, like islands in an ocean. Fig. 3.1a shows the layer structure of the experimental setup. Above a GaAs-substrate is the back contact which consists of highly doped GaAs to ensure the necessary conductivity of the contact. The InAs monolayer and the quantum dots are sandwiched between two GaAs layers which leads to a dip in the conduction band (Fig. 3.1b) and gives rise to the formation of local levels inside the InAs-dots. The AlAs/GaAs layer acts as a tunnel barrier, so that an increase of gate voltage causes only a change of the potential-form, but no current flow through the system. As the gate voltage is varied, the position of the dot-levels changes relative to the Fermi energy. This way, the number of electrons in the dot can be tuned by adjusting the applied voltage. The number of electrons in the dot also determines the label of the excitons, which are named after their total charge, indicated by a superscript. So one speaks e. g. of the X^{+1}-, X^{0}-, X^{-1}-exciton which consist of a single hole, a hole and an electron, a hole and two electrons and so on.

It is important to mention, that in the valence level, where the hole is created, the spin-orbit interaction leads to a splitting between the $J = 1/2$- and $J = 3/2$-states. The states with $J_z = \pm 3/2$ along the growth direction have the lowest zero-point energy because of their heavy mass for motion along the growth direction and are therefore the relevant levels for the optical excitations with the lowest energy. Hence, the holes h_σ have a pseudo-spin of $J_z = \pm 3/2$ and their Zeeman-splitting in a magnetic field is given by $\sigma \frac{3}{2} g_h B$.

The hole is connected to the e-level electron not only by the excitonic Coulomb attraction, but also via the exchange interaction, which, however, was neglected in this thesis. The effect of the exchange interaction would be the following: Due to the large splitting between the $|S_z| = 3/2$- and the $|S_z| = 1/2$-states, the spin-flip dynamics of the hole spin will still be frozen even when exchange interaction is taken

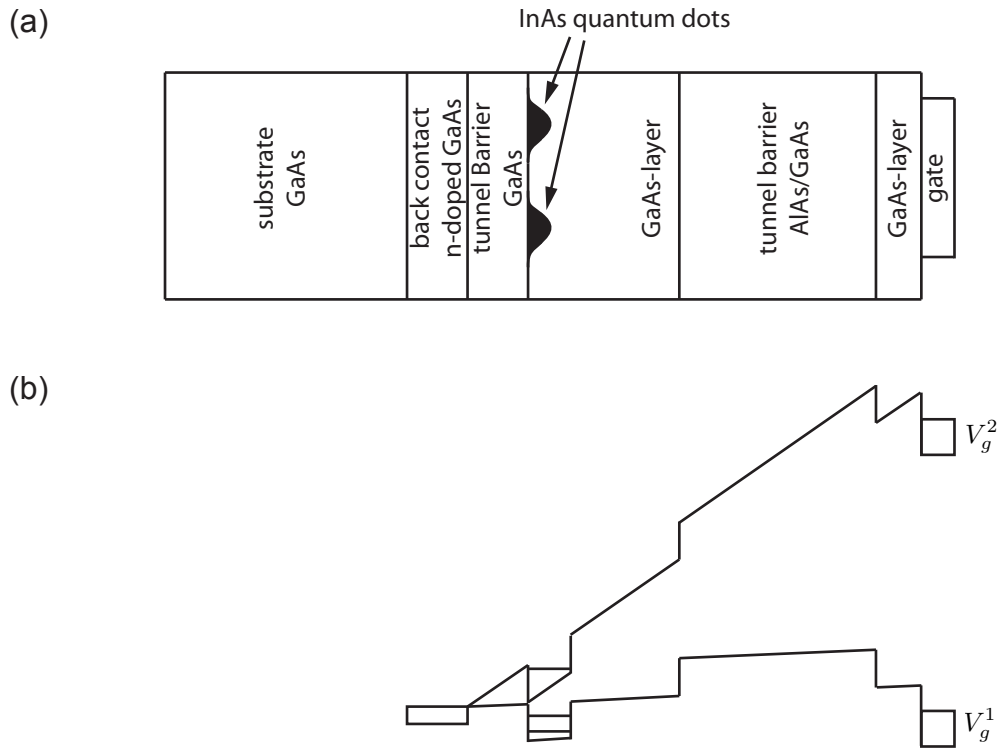

Figure 3.1: Layer structure and its band diagram. Picture from [19]. (a) Layer structure of the experimental setup. (b) The band diagram of the layer structure is shown for two different gate voltages V_g^1 and V_g^2. Increasing the gate voltage changes the number of electrons in the dot.

into account, so that the exchange interaction reduces to $J_{eh}S_e^zS_h^z$. This acts on the e-level like a magnetic field of strength $\frac{3}{2}\sigma J_{eh}$. By applying a small magnetic field in the opposite direction, the "static exchange field" can be fully compensated, so that the predictions of this thesis remain unchanged when a constant term is added to the magnetic field: $B \to B - \frac{3}{2}\sigma J_{eh}$.

In case it is nevertheless necessary to experimentally avoid the exchange interaction for some reasons, it can be eliminated in two ways. One possibility is to use the single-hole charged QD as the *initial* state; experiments on single QDs which are embedded in n-type Schottky structures have already shown that such a charged state can have lifetimes well above 100 μsec. An additional photon-absorption creates the X^{+1} trion, which consists of two holes and an electron in a local level. The holes form a singlet and due to their spins cancelling each other, their exchange interaction with the local electron vanishes. The other way to avoid the exchange interaction, is to use coupled quantum dots with indirect excitons where electron and hole have wave-functions with vanishing spatial overlap.

3.2 Recent experimental work

An optical experiment that already addressed the Kondo effect was conducted by Smith et al. [10] in 2005. They observed a spin-flip process in a quantum dot where the spin was flipped by a tunneling process between local level and reservoir, like the one shown in Fig. 2.2. Although the dot is not in a Kondo state, spin-flip tunneling between dot and reservoir is a Kondo-like interaction, which brings the experiment close to the actual optical detection of the Kondo effect.

The most recent experiment, by Dalgarno et al [11], showed very impressive results. By adjusting the gate voltage, the position of the local level relative to the Fermi energy can be changed and so it is possible to switch between the X^0- and X^{-1}-state, i. e., to change the occupation of the dot. At the experiment a sweep of the gate voltage was performed and the energy of the photon, which was emitted at the X^0- or X^{-1}-recombination, respectively, was measured. The spectra for two dots can be seen in Fig. 3.2. After recombination of the X^{-1}-exciton the dot contains one electron. Depending on gate voltage, however, the ground state of the dot has zero, single or double occupation. So, if the ground state contains zero or two electrons after the X^{-1}-recombination, the local electron is unstable with respect to tunneling from the dot into the reservoir, or from the reservoir into the dot. The hybridization between dot and reservoir due to this tunneling processes can be seen at the left and right end of the X^{-1}-lines in Fig. 3.2. These hybridizations show that tunneling connects a variety of reservoir states to the dot. A higher energy difference between the state after recombination and the ground state causes a decrease of the admixture of states. This is because if the electron tunnels from the dot to the continuum, it changes its energy by ΔE and the tunnel process therefore happens on a time scale of $\sim \hbar/\Delta E$. Only if the tunneling time is comparable to this time scale or larger, this state is part of the final state.

This setup already had all features for the dot to be in a Kondo state after absorption, however the tunnel interaction between dot and reservoir was not strong enough, yet. According to the authors this strong coupling could be achieved by narrowing the tunnel barrier, lower temperature and a higher mobility of the electrons in the reservoir.

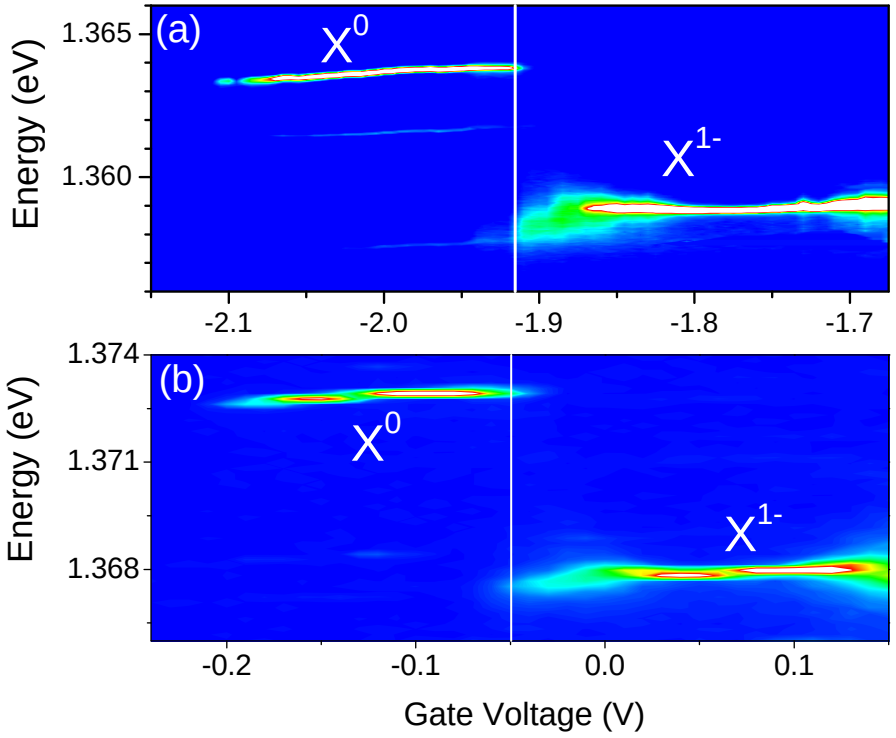

Figure 3.2: Measured photoluminescence intensity vs. gate voltage V_g from two InAs/GaAs quantum dots at nominally 4 K. The colors indicate the detector counts, the white solid lines mark the X^0 to X^{-1}-transition. Picture: courtesy of P. Dalgarno.

Chapter 4

Numerical calculations

In the 1970's K. G. Wilson developed the NRG method to solve the Kondo Hamiltonian and explain the Kondo Problem [4]. Developing an alternative method to perturbation theory was necessary to make energy scales below T_K accessible. In the following years, the NRG was adapted to several other impurity models. One of these models is the widely used Anderson model as described in [14]. This model has been solved with the NRG-method by Krishna-Murthy et al. in 1980 [20].

4.1 NRG-method

The NRG method is an iterative procedure, that numerically diagonalizes the Hamiltonians of quantum impurity models like the Anderson- or the Kondo-Hamiltonian.

For calculations concerning the excitonic Anderson model that include both the initial and final Hamiltonian, the NRG-method is applied twice, once with the e-level at position $\varepsilon^i_{e\sigma}$ and once at $\varepsilon^f_{e\sigma} = \varepsilon^i_{e\sigma} - U_{eh}$.

Thus, for our purposes it is sufficient to take the Single Impurity Anderson Model to describe the NRG method.

The SIAM-Hamiltonian is given by the following expression:

$$
\begin{aligned}
H &= H_{QD} + H_c + H_t && (4.1)\\
H_{QD} &= \sum_\sigma \varepsilon_{e\sigma} n_{e\sigma} + U n_{e\uparrow} n_{e\downarrow} && (4.2)\\
H_c &= \sum_{\vec{k}\sigma} \varepsilon_{\vec{k}\sigma} c^\dagger_{\vec{k}\sigma} c_{\vec{k}\sigma} && (4.3)\\
H_t &= \sqrt{\Gamma/\pi\rho} \sum_\sigma (e^\dagger_\sigma c_\sigma + h.c.). && (4.4)
\end{aligned}
$$

It can be written in a form with dimensionless parameters:

$$\begin{aligned} H = D \Bigg(& \int_{-1}^{1} k \sum_{\sigma} a_{k\sigma}^{\dagger} a_{k\sigma} dk \\ & + \frac{1}{D} \left(\varepsilon_{e\sigma} + \frac{1}{2} U \right) \sum_{\sigma} e_{\sigma}^{\dagger} e_{\sigma} + \frac{1}{2} \frac{U}{D} \left(\sum_{\sigma} e_{\sigma}^{\dagger} e_{\sigma} - 1 \right)^2 \\ & + \left(\frac{\Gamma}{\pi D} \right)^{1/2} \int_{-1}^{1} dk \sum_{\sigma} \left(a_{k\sigma}^{\dagger} e_{\sigma} + e_{\sigma}^{\dagger} a_{k\sigma} \right) \Bigg), \end{aligned} \tag{4.5}$$

where $k \equiv \varepsilon / D$ is a dimensionless parameter (not the wave-vector $\vec{k}$), which describes the energy normalized by bandwidth and $a_{k\sigma} \equiv \sqrt{D} a_{\varepsilon\sigma}$. $a_{k\sigma}$ ($a_{k\sigma}^{\dagger}$) and $a_{\varepsilon\sigma}$ ($a_{\varepsilon\sigma}^{\dagger}$) are annihilation (creation) operators that annihilate (create) an electron in the FR which has energy k (or ε, respectively) and spin σ.

To calculate properties of the combined system QD-reservoir it is necessary to discretize the energy spectrum in an efficient way to reduce computation costs. Therefore, one uses a logarithmic discretization scheme. This is due to the facts that: (i) all energy scales have to be taken into account for the calculation of physical properties and (ii) low energies play a major role in impurity systems and logarithmic discretization has a finer resolution for low energies.

To discretize the energy spectrum as described above, a parameter $\Lambda > 1$ is introduced and the energy spectrum is divided into intervals determined by Λ, as shown in Fig. 4.1, where the nth interval extends from $\Lambda^{-(n+1)}$ to Λ^{-n}. Within these intervals one can set up a Fourier series which constitutes a complete set of orthonormal functions and which therefore spans the whole k space:

$$\psi_{np}^{\pm}(k) \equiv \begin{cases} \frac{\Lambda^{n/2}}{(1-\Lambda^{-1})^{1/2}} e^{\pm i \omega_n p k} & \text{if } \Lambda^{-(n+1)} < \pm k < \Lambda^{-n} \\ 0 & \text{if } \pm k \text{ is outside the above interval} \end{cases} \tag{4.6}$$

$n = 0, 1, 2, ...$ is the interval index, p is the Fourier harmonic index and takes integer values from $-\infty$ to $+\infty$. Each interval occurs twice, once for positive and once for negative k-values. The superscript $\pm$ indicates whether one refers to the interval in the positive or in the negative k-part. ω_n is the Fourier frequency for the nth interval and is given by:

$$\omega_n \equiv \frac{2\pi}{\Lambda^{-n} - \Lambda^{-(n+1)}} = \frac{2\pi \Lambda^n}{1 - \Lambda^{-1}}. \tag{4.7}$$

The operators $a_{k\sigma}$ can now be expressed in this basis.

$$a_{k\sigma} = \sum_{np} [a_{np\sigma} \psi_{np}^{+}(k) + b_{np\sigma} \psi_{np}^{-}(k)], \tag{4.8}$$

$$a_{np\sigma} = \int_{-1}^{+1} dk [\psi_{np}^{+}(k)]^* a_{k\sigma}, \; b_{np\sigma} = \int_{-1}^{+1} dk [\psi_{np}^{-}(k)]^* a_{k\sigma}. \tag{4.9}$$

The $a_{np\sigma}$- and $b_{np\sigma}$-operators constitute a complete set of independent and discrete electron operators which fulfill standard anti-commutation rules: $[a_{np\sigma}, a_{n'p'\sigma'}^{\dagger}]_+ = \delta_{n,n'} \delta_{p,p'} \delta_{\sigma,\sigma'}$.

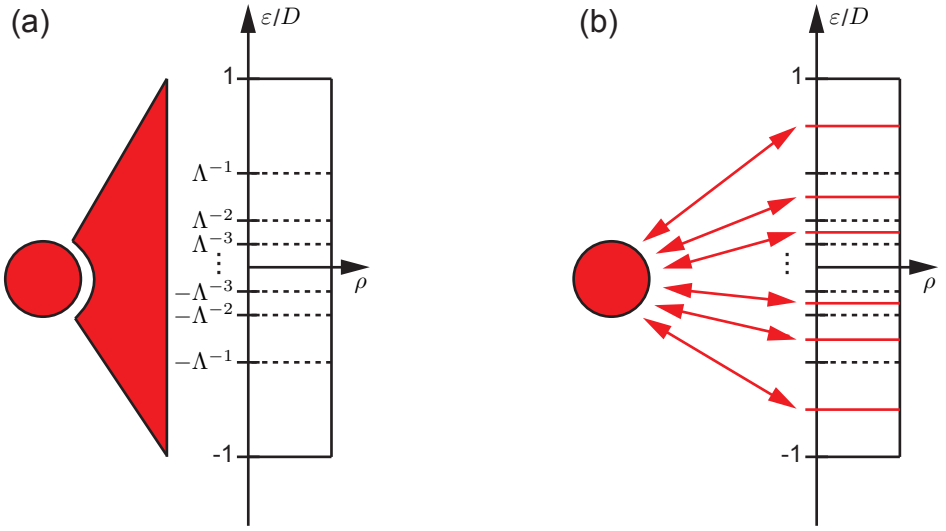

Figure 4.1: Logarithmic discretization of the energy spectrum of the reservoir. Picture from [21]. (a) The impurity (red dot) couples to the whole reservoir where coupling strength does not depend on energy. The reservoir is logarithmically divided into ever smaller intervals indicated by dashed lines. (b) Each energy interval is represented by a single energy value which is taken to be the mean value of the interval. The coupling strength to a discrete energy value is then proportional to the interval size and therefore decreases for smaller energy values.

With these operators, the Hamiltonian (4.5) can be expressed as a discrete sum. To do this, one uses the following relations, which can easily be verified:

$$\begin{aligned}\int_{-1}^{+1} k \sum_{\sigma} a_{k\sigma}^{\dagger} a_{k\sigma} dk &= \frac{1}{2}\left(1+\Lambda^{-1}\right) \sum_{n,p,\sigma} \Lambda^{-n} \left(a_{np\sigma}^{\dagger} a_{np\sigma} - b_{np\sigma}^{\dagger} b_{np\sigma}\right) \\ &\quad + \frac{1-\Lambda^{-1}}{2\pi i} \sum_{n,p\neq p',\sigma} \left(a_{np\sigma}^{\dagger} a_{np'\sigma} - b_{np\sigma}^{\dagger} b_{np'\sigma} \exp\left(\frac{2\pi i(p'-p)}{1-\Lambda^{-1}}\right)\right), \\ \int_{-1}^{+1} \sum_{\sigma} a_{k\sigma} dk &= (1-\Lambda)^{1/2} \sum_{n,\sigma} \Lambda^{-n/2} (a_{n0\sigma} + b_{n0\sigma}).\end{aligned} \tag{4.10}$$

Inserting Eq. (4.10) in Eq. (4.5) reveals that the impurity couples only to the operators $a_{n0\sigma}$ and $b_{n0\sigma}$ directly. The operators $a_{np\sigma}$ and $b_{np\sigma}$ with $p \neq 0$ are only connected indirectly to the impurity by the second term in Eq. (4.10) which couples them to $a_{n0\sigma}$ and $b_{n0\sigma}$. Since this term has a prefactor of $\left(1-\Lambda^{-1}\right)/2\pi$, this indirect coupling will be very small if Λ is close to 1. Because of that the terms in Eq. (4.10) with $a_{np\sigma}$ and $b_{np\sigma}$ can be dropped for $p \neq 0$. This turns out to be a good approximation for sufficiently small Λ, e. g. $\Lambda \leq 3$.

By using this approximation, dropping the subscript "0" of the operators $a_{n0\sigma}$

and $b_{n0\sigma}$ and introducing the operators

$$f_{0\sigma} = \left[\frac{1}{2}\left(1-\Lambda^{-1}\right)\right]^{1/2} \sum_{n=0}^{\infty} \Lambda^{-n/2} \sum_{\sigma} \left(a_{n\sigma} + b_{n\sigma}\right) \equiv \frac{1}{\sqrt{2}} \int_{-1}^{+1} dk a_{k\sigma}, \tag{4.11}$$

with $[f_{0\sigma}, f^{\dagger}_{0\sigma'}] = \delta_{\sigma,\sigma'}$ the Hamiltonian can be now written as:

$$\begin{aligned} \frac{H}{D} = & \frac{1}{2}\left(1+\Lambda^{-1}\right) \sum_{n=0}^{\infty} \Lambda^{-n} \left(a^{\dagger}_{n\sigma} a_{n\sigma} - b^{\dagger}_{n\sigma} b_{n\sigma}\right) \\ & + \frac{1}{D}\left(\varepsilon_{e\sigma} + \frac{1}{2}U\right) e^{\dagger}_{\sigma} e_{\sigma} + \frac{1}{2}\frac{U}{D}\left(e^{\dagger}_{\sigma} e_{\sigma} - 1\right)^2 \\ & + \left(\frac{2\Gamma}{\pi D}\right)^{1/2} \left(f^{\dagger}_{0\sigma} e_{\sigma} + e^{\dagger}_{\sigma} f_{0\sigma}\right). \end{aligned} \tag{4.12}$$

Now one performs a unitary transformation from the operators $(a_{n\sigma}, b_{n\sigma})$ to a new orthonormal set of operators $f_{n\sigma}$ at which $f_{0\sigma}$ remain unchanged. Because the term in Eq. (4.12) that describes the kinetic energy of the electrons is diagonal in $(a_{n\sigma}, b_{n\sigma})$, a transformation will create non-diagonal matrix elements, i. e. a transformation will couple the operators $(f_{n\sigma})$ to one another. The trick is to choose a transformation which couples $f_{n\sigma}$ only to its nearest neighbors $f_{(n\pm1)\sigma}$. After this transformation [20] one gets the following expression, the so-called Hopping Hamiltonian:

$$\begin{aligned} \frac{H}{D} = & \frac{1}{2}\left(1+\Lambda^{-1}\right) \sum_{n=0}^{\infty} \Lambda^{-n/2} \xi_n \sum_{\sigma} \left[f^{\dagger}_{n\sigma} f_{(n+1)\sigma} + f^{\dagger}_{(n+1)\sigma} f_{n\sigma}\right] \\ & + \frac{1}{D}\left(\varepsilon_{e\sigma} + \frac{1}{2}U\right) \sum_{\sigma} e^{\dagger}_{\sigma} e_{\sigma} + \frac{1}{2}\frac{U}{D}\left(\sum_{\sigma} e^{\dagger}_{\sigma} e_{\sigma} - 1\right)^2 \\ & + \left(\frac{2\Gamma}{\pi D}\right)^{1/2} \sum_{\sigma} \left(f^{\dagger}_{0\sigma} e_{\sigma} + e^{\dagger}_{\sigma} f_{0\sigma}\right), \end{aligned} \tag{4.13}$$

with

$$\xi_n = (1-\Lambda^{-n-1})(1-\Lambda^{-2n-1})^{-1/2}(1-\Lambda^{-2n-3})^{-1/2}, \tag{4.14}$$

which converge to one in the limit of large n.

This Hamiltonian can be represented by a semi-infinite chain, the so-called Wilson chain (Fig. 4.1). The chain starts with the impurity which is then coupled to the site that corresponds to the eigenstate of the operators $f^{\dagger}_{0\sigma}$ and $f_{0\sigma}$. This site is then coupled to the site that corresponds to the eigenstate of $f_{1\sigma}$, this one is coupled to the f_2-site and so on. As n increases, the coupling becomes proportional to $\Lambda^{-n/2}$, it decays exponentially.

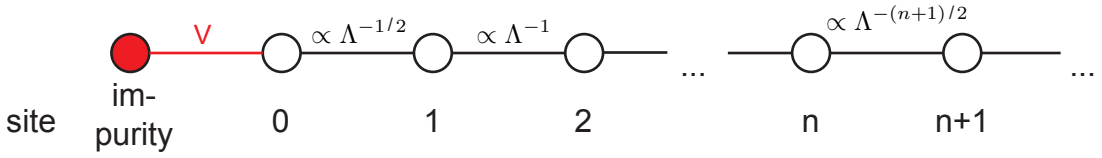

Figure 4.2: Wilson chain. The original Hamiltonian can be mapped on a semi-infinite chain Hamiltonian that starts with the impurity and where each site is connected only to its nearest neighbors by exponentially decreasing coupling strength. Due to the decreasing coupling strength, the contribution of new sites goes to zero for large n.

With help of the Hamiltonians H_N,

$$\begin{aligned} H_N \equiv \Lambda^{(N-1)/2} \Bigg[& \sum_{n=0}^{N-1} \Lambda^{-n/2} \xi_n \sum_{\sigma} \left(f_{n\sigma}^{\dagger} f_{(n+1)\sigma} + f_{(n+1)\sigma}^{\dagger} f_{n\sigma} \right) \\ & + \widetilde{\Gamma}^{1/2} \sum_{\sigma} \left(f_{0\sigma}^{\dagger} e_{\sigma} + e_{\sigma}^{\dagger} f_{0\sigma} \right) \\ & + \widetilde{\delta}_e \sum_{\sigma} e_{\sigma}^{\dagger} e_{\sigma} + \widetilde{U} \left(\sum_{\sigma} e_{\sigma}^{\dagger} e_{\sigma} - 1 \right)^2 \Bigg], \end{aligned} \tag{4.15}$$

that have a finite number of elements determined by N, the Hopping Hamiltonian can be expressed as:

$$H = \lim_{N \to \infty} \frac{1}{2} \left(1 + \Lambda^{-1} \right) D \Lambda^{-(N-1)/2} H_N, \tag{4.16}$$

where the following constants were defined for simplification of Eq. (4.15):

$$\widetilde{\delta}_e \equiv \left(\frac{2}{1+\Lambda^{-1}} \right) \frac{1}{D} \left(\varepsilon_{e\sigma} + \frac{1}{2} U \right) \equiv \widetilde{\varepsilon}_e + \widetilde{U} \tag{4.17}$$

$$\widetilde{U} \equiv \left(\frac{2}{1+\Lambda^{-1}} \right) \frac{U}{2D} \tag{4.18}$$

$$\widetilde{\Gamma} \equiv \left(\frac{2}{1+\Lambda^{-1}} \right)^2 \frac{2\Gamma}{\pi D}. \tag{4.19}$$

From Eq. (4.15) it follows that the Hamiltonians H_N fulfill the recursion relation:

$$H_{N+1} = \Lambda^{1/2} H_N + \xi_N (f_{N\sigma}^{\dagger} f_{N+1\sigma} + f_{N+1\sigma}^{\dagger} f_{N\sigma}). \tag{4.20}$$

Due to this recursion relation it is possible to create a recursive procedure from which one can calculate the Eigenstates and the corresponding energies of H_{N+1}, if the ones from H_N are known.

To apply this procedure on the Hamiltonian one needs a set of eigenstates and energy levels as a starting point. These can be obtained from

$$H_0 = \Lambda^{-1/2}\left[\widetilde{\delta}_e e^\dagger_\sigma e_\sigma + \widetilde{\Gamma}^{1/2}(f^\dagger_{0\sigma} e_\sigma + e^\dagger_\sigma f_{0\sigma}) + \widetilde{U}(e^\dagger_\sigma e_\sigma - 1)^2\right]. \tag{4.21}$$

At the recursive procedure $|l, N\rangle$ is the eigenstate of H_N with energy-index l. If the states $|l, N\rangle$ are known, one also knows the matrix elements $\langle l, N|f^\dagger_{n\sigma}|l', N\rangle$

With the states $|l, N\rangle$ it is possible to create the following new states:

$$\begin{aligned}
|1, l, N\rangle &\equiv |l, N\rangle \\
|2, l, N\rangle &\equiv f^\dagger_{N+1\uparrow}|l, N\rangle \\
|3, l, N\rangle &\equiv f^\dagger_{N+1\downarrow}|l, N\rangle \\
|4, l, N\rangle &\equiv f^\dagger_{N+1\uparrow} f^\dagger_{N+1\downarrow}|l, N\rangle.
\end{aligned} \tag{4.22}$$

$|i, l, N\rangle$ $(i = 1, 2, 3, 4)$ are an orthonormal basis for H_{N+1} and thus it is possible to calculate its matrix elements $\langle i', l', N|H_{N+1}|i, l, N\rangle$.

At each Hamiltonian H_{N+1} the term $\xi_N \sum_\sigma (f^\dagger_{N\sigma} f_{N+1\sigma} + f^\dagger_{N+1\sigma} f_{N\sigma})$ adds a new site to the Wilson chain that corresponds to an energy scale of $\Lambda^{-N/2}$. Once the energy scale of interest is reached, one stops applying the recursion relation and the obtained eigenstates and -energies can be used for further calculations.

As can be seen from Eq. (4.22) every time a new site is added to the Wilson chain, the Hilbert space of the system is multiplied by 4, the dimension of the state space of a site. To prevent the Hilbert space from growing exponentially with the number of sites, only the M_K states that are lowest in energy are kept at each iteration, where M_K is typically chosen between 256 and 1024. Calculation time is further reduced by using some symmetries of the system, namely the fact, that the z-component of the total spin and the particle number are conserved, so that the state space can be divided into subspaces that correspond to the quantum numbers of the problem.

There have been developments in the past years how the NRG-determined eigenstates are used best to calculate physical quantities. The first approach by Wilson was to use only the states of iteration n which corresponds to the energy scale $\Lambda^{-n/2}$ to describe the physics at that scale. This step involves several approximations which are necessary to handle the problem that the states obtained at one NRG-iteration do not constitute a complete basis.

A newer concept, which was developed by [22], [23] and [24] was used in this thesis. There, the idea is not only to make use of the states at a certain NRG-iteration, but to use an approximate but complete basis set of states. The trick to obtain such a basis, is to keep the states that are discarded after each iteration (see Fig. 4.1ab). When the iterations are completed, there are only discarded states left, which form a complete set of basis states (Fig. 4.1b, right part). Eigenstates at iteration $n < N$ are then considered as d^{N-n}-fold degenerate eigenstates of the full chain. The first clean application of the complete state space to the calculation of spectral correlation functions was given in [24]. Specifically, it includes an expansion of the density matrix in the complete state space, which is crucial for finite temperature calculations.

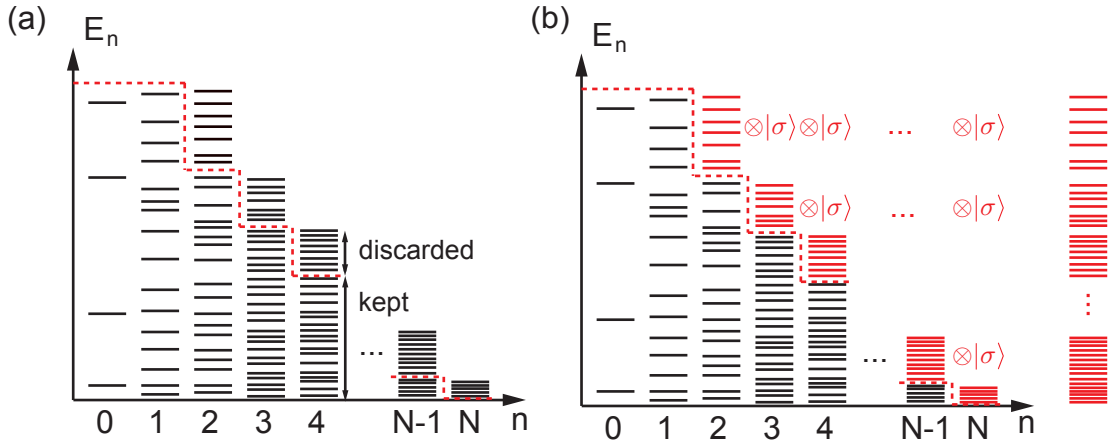

Figure 4.3: Obtaining a complete basis set of states. Picture from [25]. The figures show the energy spectra for each iteration. (a) As soon as the dimension of the Hilbert Space exceeds a certain number M_K, only the lowest M_K states are kept at an iteration, the rest of the states is discarded. (b) The discarded states at iteration n are taken to be (N-n)-fold degenerate, indicated by $|\sigma\rangle$ that represents the Hilbert space of one site. After the total number of iterations N a set of complete basis states remains (shown after the last iteration).

4.2 Energy flow diagram

To get insight which energy scales determine the physics of the system, it is instructive to examine how the energy spectrum of the kept-states, which are used for the iterative diagonalization, varies with increasing iteration. Since the Wilson chain has exponentially decaying coupling strength, the level spacing between the lowest-energy states also becomes exponentially smaller for each new site that is added to the chain (see Fig. 4.2a). If these energies are rescaled by multiplication with $\Lambda^{-(n-1)/2}$ (Fig. 4.2b), one obtains a so-called energy flow diagram 4.2b. These diagrams illustrate, that the rescaled energy spectrum has certain fixed points, i. e., regimes where the rescaled energies do not change any more at successive iterations. These fixed points are separated by crossovers of several iterations which happen at characteristic energy scales (indicated by thick yellow lines in Fig. 4.2b). A change of the rescaled energy spectrum corresponds to a change in the physical processes that are relevant at that energy scale. In [20] it is shown that the Anderson model exhibits three different fixed points, the Free Orbital- (FO), the Local Moment- (LM) and the Strong Coupling fixed point (SC), see Fig. 4.2b. In 5.3 it is shown that these fixed points govern the details of the absorption lineshape.

4.3 Calculations using NRG-results

The complete set of approximate many-body eigenstates of the full Hamiltonian can be used to evaluate spectral functions given in Lehmann representation which are perfectly suited for numerical calculations involving eigenengergies and -states from

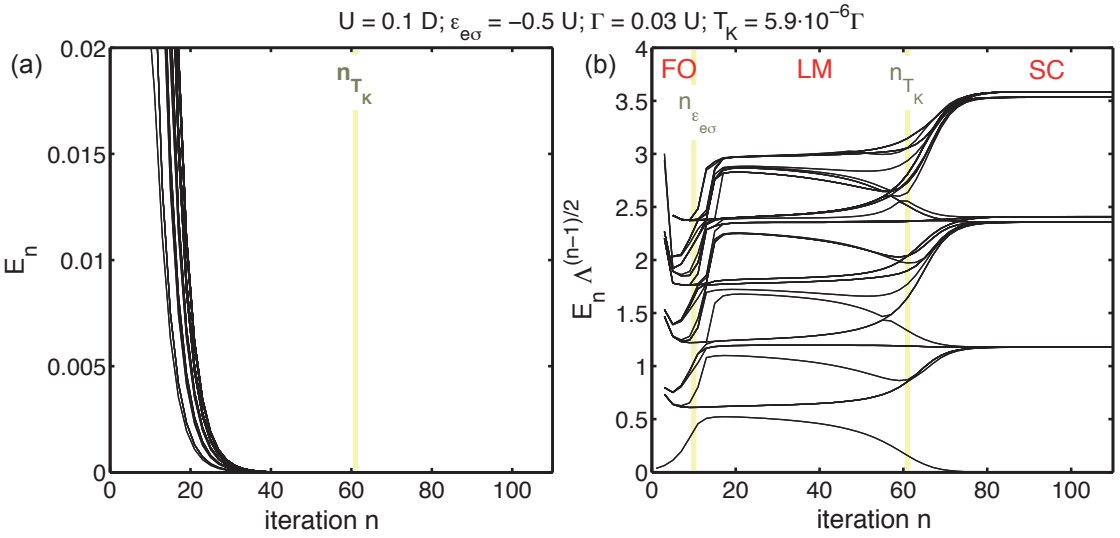

Figure 4.4: Spectrum of 100 lowest eigenenergies at each iteration. (a) Energies are not rescaled. Adding a site with exponentially decaying coupling strength to the Wilson chain causes the exponential descent of the lowest eigenenergies. (b) If the energies are rescaled one obtains an energy flow diagram that shows the fixed points of the system (labelled with FO, LM, SC and separated by yellow lines). Different fixed points correspond to different physical properties of the system.

an iterative NRG-calculation (= NRG-run).

General spectral functions written in Lehmann representation have the following form:

$$\mathcal{A}_{BC}(\omega) = \sum_{mn} \frac{e^{-\beta E_m}}{Z} \langle m|B|n\rangle\langle n|C|m\rangle \delta(\omega - (E_n - E_m)), \tag{4.23}$$

where B and C are local operators acting on the dot. Eq. (4.23) can be directly evaluated in the complete many body basis. This approach which makes use of the full density matrix (FDM) instead of the density matrix of a single shell, is known as FDM-NRG [24].

4.3.1 Absorption spectrum

The absorption spectrum is calculated making use of Fermi's Golden Rule (FGR). This well-known formula can be obtained by perturbation theory and yields the transition probability per unit time to make a transition from initial state $|m\rangle$ into one of the possible final states $|n\rangle$:

$$p_{mn} = \frac{2\pi}{\hbar} \sum_n |\langle n|H_{pert}|m\rangle|^2, \tag{4.24}$$

where H_{pert} is the perturbation Hamiltonian. In the case of photon absorption at a two-level system, it is given by $H_L = \gamma(e_\sigma^\dagger h_{\bar{\sigma}}^\dagger + h.c.)$ (see Eq. (2.10)).

The absorption lineshape is therefore proportional to

$$\begin{aligned} A(\omega_L) &= \frac{2\pi}{|\gamma|^2} \sum_n |{}_f\langle n|H_{pert}|G\rangle_i|^2 \delta(\omega_L - E_n^f + E_G^i) \\ &= 2\pi \sum_n |{}_f\langle n|e_\sigma^\dagger|G\rangle_i|^2 \delta(\omega_L - E_n^f + E_G^i), \end{aligned} \tag{4.25}$$

where $|G\rangle_i$ is the ground state of the initial Hamiltonian, $|n\rangle_f$ are the eigenstates of the final Hamiltonian, E_G^i and E_n^f are the corresponding energies, and ω_L is the laser frequency ($\hbar$ is set to 1).

To obtain the absorption for $T \neq 0$, the transition probabilities according to Fermi's Golden Rule have to be summed up for different initial states, which are weighted with their Boltzmann factors $\rho_m^i = e^{-\beta E_m^i}/Z^i$:

$$A_\sigma(\nu) = 2\pi \sum_{mn} \rho_m^i |{}_f\langle n|e_\sigma^\dagger|m\rangle_i|^2 \delta(\omega_L - E_n^f + E_m^i), \tag{4.26}$$

with detuning $\nu = \omega_L - \omega_{th}$, where ω_{th} is the threshold frequency below which at $T = 0$ no photons can be absorbed, as is shown in 5.3.

Since Eq. (4.26) expresses the absorption rate in Lehmann representation, NRG can be used to evaluate it [24]. Because of the two different Hamiltonians H^i and H^f, two NRG runs are needed to determine all energy values and eigenstates necessary to calculate the absorption spectrum, one run for each Hamiltonian. The threshold frequency ω_{th}, above which absorption starts is given by the difference of the ground state energies of the initial and final Hamiltonian: $\omega_{th} \equiv E_G^f - E_G^i$.

To reduce computing time, the discrete data of $A(\nu)$ (which is a sum of δ-functions) is binned to reduce the number of data points without relevant loss of accuracy. To accommodate the logarithmic discretization, the binning is chosen to be logarithmic also, with typically 256 bins per decade. After that, the discrete data is smoothed with a log-Gaussian broadening function [24]. Its width is determined by a broadening parameter α whose value is usually between $\alpha = 0.4 - 0.6$. To connect positive and negative frequencies, a regular Gaussian with width ω_0 is used for broadening for frequencies $\nu < \omega_0$, where ω_0 is roughly a factor 2 smaller than the smallest energy scale in the problem. At ω_0 the broadening function does not change from log-Gaussian to Gaussian abruptly, but it is smoothly interpolated between the two broadening functions.

4.3.2 Occupations

The mean occupations with spin σ of the local level $n_{e\sigma}$ can be calculated with NRG,

$$n_{e\sigma}^a = \sum_m \rho_{m\,a}^a \langle m|e_\sigma^\dagger e_\sigma|m\rangle_a, \tag{4.27}$$

where $a = i, f$; depending on whether the mean occupation is calculated for the initial or the final state. This term of the form of Eq. (4.23) and can be easily evaluated with NRG.

The probability for the local level to be occupied only with a σ-electron, but with no $\bar{\sigma}$-electron, $n_{e,\sigma 0}$, can be obtained by first calculating the probability that the local level is doubly occupied:

$$\begin{aligned} n_{e,\sigma\bar{\sigma}} &= \sum_m \rho_m^a \, {}_a\langle m|e_{\bar{\sigma}}^\dagger e_{\bar{\sigma}} e_\sigma^\dagger e_\sigma|m\rangle_a \\ &= \sum_{mn} \rho_m^a \, {}_a\langle m|e_{\bar{\sigma}}^\dagger e_\sigma^\dagger|n\rangle_a \, {}_a\langle n|e_{\bar{\sigma}} e_\sigma|m\rangle_a \\ &= \sum_{mn} \rho_m^a |_a\langle n|e_{\bar{\sigma}} e_\sigma|m\rangle_a|^2. \end{aligned} \tag{4.28}$$

It is then possible to calculate $n_{e,\sigma 0}$ from existing quantities by constructing the difference between $n_{e\sigma}$ and $n_{e,\sigma\bar{\sigma}}$:

$$n_{e,\sigma 0} = n_{e\sigma} - n_{e,\sigma\bar{\sigma}} \tag{4.29}$$

4.3.3 Time-dependent NRG

At an absorption process, an exciton is created at $t = 0$. This is modelled by changing the position of the local level from $\varepsilon_{e\sigma}^i$ to $\varepsilon_{e\sigma}^f$ and by the sudden creation of a σ-electron at the e-level. Therefore, absorption can only take place if there is no σ-electron in the initial state.

The fact that absorption can take place only for some initial states, can be seen at the transformation of the density matrix to the projected density matrix $\hat{\rho}_P$.

$$\hat{\rho}^{\mathrm{i}} \equiv \sum_m |m\rangle_{\mathrm{i}} (\rho_m^{\mathrm{i}}) \, {}_{\mathrm{i}}\langle m| \rightarrow \hat{\rho}_{\mathrm{p}} \equiv \sum_m (e_\sigma^\dagger |m\rangle_{\mathrm{i}})(\rho_m^{\mathrm{i}}) \, ({}_{\mathrm{i}}\langle m|e_\sigma) = e_\sigma^\dagger \hat{\rho}^{\mathrm{i}} e_\sigma \ . \tag{4.30}$$

whose norm is no longer 1, but is reduced by the initial occupation of the σ-electron

$$\mathrm{Tr}\hat{\rho}_{\mathrm{p}} = \mathrm{Tr}\left(\hat{\rho}^{\mathrm{i}} e_\sigma e_\sigma^\dagger\right) = 1 - \bar{n}_{\mathrm{e}\sigma}^{\mathrm{i}} \ . \tag{4.31}$$

Immediately after the absorption process, the e-level occupations for spin σ' are:

$$\mathrm{Tr}(\hat{\rho}_{\mathrm{p}} \hat{n}_{\mathrm{e}\sigma'}) = \begin{cases} \bar{n}_{\mathrm{e},00}^{\mathrm{i}} + \bar{n}_{\mathrm{e},0\bar{\sigma}}^{\mathrm{i}} = 1 - \bar{n}_{\mathrm{e}\sigma}^{\mathrm{i}} & \text{for } \sigma' = \sigma \ , \\ \bar{n}_{\mathrm{e},0\bar{\sigma}}^{\mathrm{i}} & \text{for } \sigma' = \bar{\sigma} \ , \end{cases} \tag{4.32}$$

where $\bar{n}_{\mathrm{e},00}^{\mathrm{i}}$ and $\bar{n}_{\mathrm{e},0\bar{\sigma}}^{\mathrm{i}}$ are the initial probabilities for the e-level to have been completely empty (00), or to have been occupied with no σ-electron but only with a $\bar{\sigma}$-electron ($0\bar{\sigma}$).

When examining the time evolution, it is assumed that an absorption process has just taken place at $t = 0$. Therefore the starting density matrix is the normalized projected density matrix $\hat{\rho}_{\mathrm{p}}^{\mathrm{f}} = \hat{\rho}_{\mathrm{p}}/[1 - \bar{n}_{\mathrm{e}\sigma}^{\mathrm{i}}]$.

After an absorption process the system is described by the final Hamiltonian H^f: $\hat{\rho}_{\mathrm{p}}^{\mathrm{f}}(t) \equiv e^{-iH^{\mathrm{f}}t} \hat{\rho}_{\mathrm{p}}^{\mathrm{f}} e^{iH^{\mathrm{f}}t}$ and the expectation value of an observable $\hat{B}$ at time t is given by $\widetilde{B}(t) = \mathrm{Tr}\left(\hat{\rho}_{\mathrm{p}}^{\mathrm{f}}(t)\hat{B}\right)$.

To calculate $\widetilde{B}(t)$, the Fourier-transformed $\widetilde{\mathcal{B}}(\omega) = \int dt\ e^{i\omega t}\widetilde{B}(t)$ is calculated, since it can be written in Lehmann representation and can therefore be easily calculated with NRG (see Eq. (4.23)).

$$\widetilde{\mathcal{B}}(\omega) = \sum_{m,n} {}_{\mathrm{f}}\langle m|\hat{\rho}_{\mathrm{p}}^{\mathrm{f}}|n\rangle_{\mathrm{f}\,\mathrm{f}}\langle n|\hat{B}|m\rangle_{\mathrm{f}} \cdot 2\pi\delta\left(\omega - E_m^{\mathrm{f}} + E_n^{\mathrm{f}}\right). \tag{4.33}$$

The final $\widetilde{\mathcal{B}}(\omega)$-function is obtained by binning and smoothing the discrete $\widetilde{\mathcal{B}}(\omega)$-data as described in 4.3.1. $\widetilde{B}(t)$ is then calculated by Fourier-transforming the smooth $\widetilde{\mathcal{B}}(\omega)$-function to the time domain.

4.3.4 Bulk magnetic field

The effect of a magnetic field *on the dot* is simple: it splits the e-level according to $\varepsilon_{e\sigma} = \varepsilon_e + \frac{1}{2}\sigma g_e B$. For the electrons in the reservoir (= the bulk), the case is a little more complicated. This is because the energy spectrum of the reservoir is continuous and the discrete energy levels needed for an NRG-run cannot be just shifted (as for the e-level), since NRG requires high resolution *close to zero energy.*

So to take a magnetic field at the reservoir into account, the DOS is first shifted with respect to the Fermi-level and discretized afterwards (see Fig. 4.5). The DOS is shifted by $+1/2g_eB$ for spin up and by $-1/2g_eB$ for spin down. Then the following energy intervals are logarithmically discretized: $[0; D + 1/2g_eB], [-D + 1/2g_eB; 0]$ for spin up and $[0; D - 1/2g_eB], [-D - 1/2g_eB; 0]$ for spin down respectively, where the resolution now again is highest for values close to zero (see Fig. 4.5). This way one can maintain a logarithmic discretization scheme at which the Wilson chain has still exponentially decaying coupling strength, which is essential for the application of the NRG-method, while taking into account the fact that the spin-up and -down bands have been shifted relative to each other.

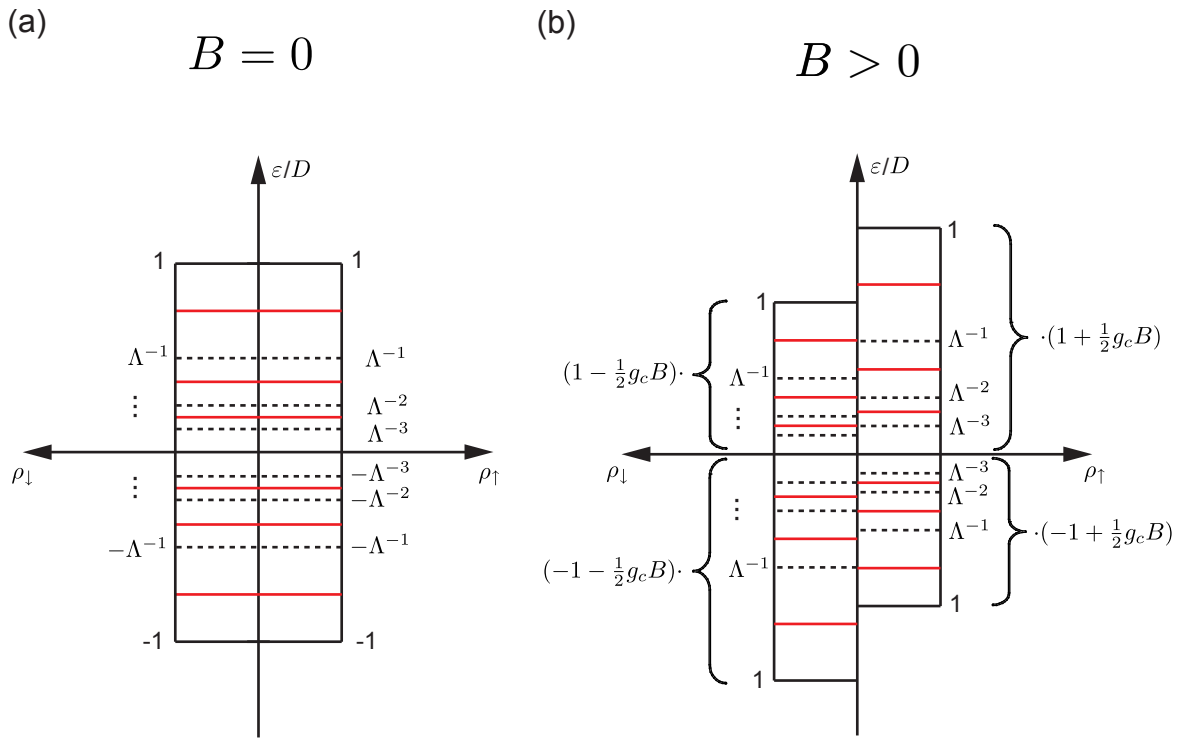

Figure 4.5: NRG-discretization for bulk magnetic field. (a) Logarithmic discretization when no magnetic field is applied. (b) To account for a magnetic field in the reservoir, the DOS is shifted with respect to the Fermi-Level and afterwards the intervals indicated by curly brackets are logarithmically discretized. The resulting Wilson chain has exponentially decaying coupling strength which makes NRG applicable.

Chapter 5

Results

5.1 Occupation of Quantum Dot

To get a basic understanding of the physics at an absorption process, it is instructive to look at the occupation of the quantum dot. The occupation of the e-level is determined by the parameters $\varepsilon^a_{e\sigma}$, Γ and U, where the position of the e-level $\varepsilon^a_{e\sigma}$ depends on further parameters like excitonic Coulomb attraction U_{eh} and magnetic field B. Fig. 5.1 shows how the initial and final occupation of the dot changes while performing a sweep of the e-level (since U_{eh} is kept constant, this means sweeping both $\varepsilon^i_{e\sigma}$ and $\varepsilon^f_{e\sigma}$ simultaneously).

As $\varepsilon^f_{e\sigma}$ is increased, the occupation changes from 2 (for $\varepsilon^f_{e\sigma} \lesssim -U$) to 1 for (for $-U \lesssim \varepsilon^f_{e\sigma} \lesssim 0$) and finally goes to zero (for $\varepsilon^f_{e\sigma} \gtrsim 0$). The regime where the occupation changes between two integer values, the so-called "mixed valence regime" has a width of several Γ. The smaller the mixed valence regime the more concise are the plateaus of n^i_e and n^f_e. The change of occupation $\Delta n_e = n^f_e - n^i_e$ is the difference between n^f_e and n^i_e. By looking at n^f_e and n^i_e at Fig. 5.1, it becomes clear, that there are always two regions where the value of Δn_e increases above zero (and approaches 1 in the limit of small Γ). Between these two regions Δn_e can either increase or decrease, depending on whether $U_{eh} < U$ (Fig. 5.1a) or $U_{eh} > U$ (Fig. 5.1b).

For most of the following calculations, the Coulomb attraction is chosen to be $U_{eh} = 5/4U$ as in Fig. 5.1b, since first, for most experimental realizations, U_{eh} is slightly larger than U, and second, it shows that the results are valid not only for $U_{eh} = U$, but for more general parameter values, too. Further, for $\varepsilon^f_{e\sigma}$ a value is chosen where the curve of Δn_e has its right plateau at $\Delta n_e \approx 1$. This regime is examined for two reasons: (i) the dot is nearly unoccupied in the initial state, so that photon absorption can take place and (ii) it is singly occupied after absorption which is necessary for the dot to be in a Kondo state.

For zero magnetic field, the $\sigma = \uparrow$- and $\sigma = \downarrow$ -occupations are equal. Although for $B \neq 0$ they differ as can be seen in Fig. 5.2a, the total occupations $n^i_e = n^i_{e\uparrow} + n^i_{e\downarrow}$ and $n^f_e = n^f_{e\uparrow} + n^f_{e\downarrow}$ stay the same. This changes when B exceeds Γ; then the splitting between the two e-levels becomes too large and tunneling is suppressed. Therefore spin-fluctuations of the dot are no longer possible and the electron occupying the e-level has a well-defined spin (Fig. 5.2b). The spin-asymmetry in occupation for nonzero B-field has dramatic consequences on the absorption spectrum, as shown

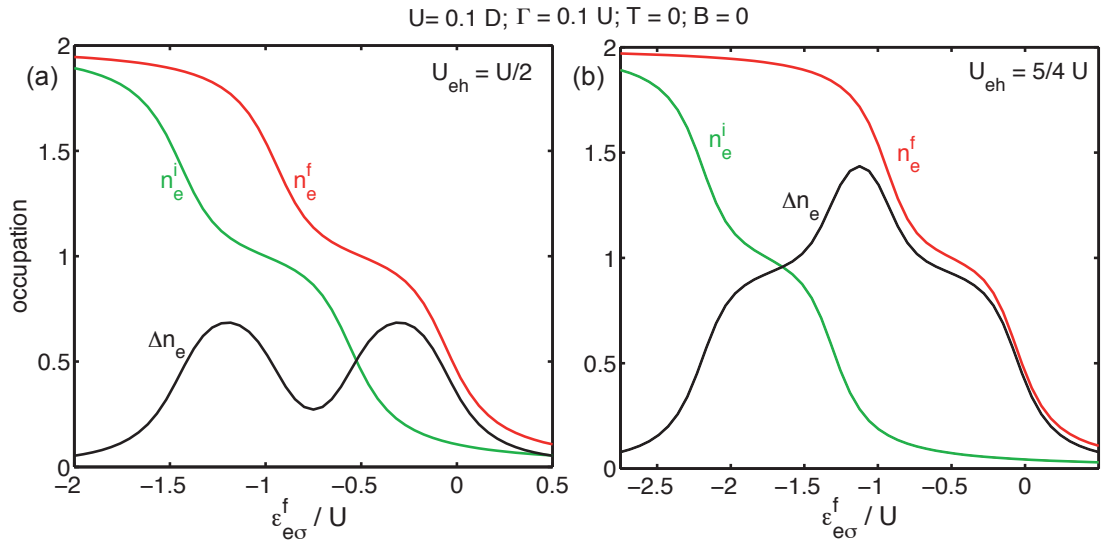

Figure 5.1: Initial and final occupations of the QD, n_e^i and n_e^f, and their difference $\Delta n_e = n_e^f - n_e^i$ as function of $\varepsilon_{e\sigma}^f$, for (a) $U_{eh} < U$ and (b) $U_{eh} > U$. As the position of the e-level $\varepsilon_{e\sigma}^f$ is increased, the initial and final occupations decrease from 2 to 1 and then to zero.

in 5.3.3.

5.2 Time evolution of charge and spin after absorption

As shown in section 4.3.1, the absorption spectrum can be calculated according to Fermi's Golden Rule: $A_\sigma(\nu) = 2\pi \sum_{mn} \rho_m^i |_f\langle n|e_\sigma^\dagger|m\rangle_i|^2 \delta(\omega_L - E_n^f + E_m^i)$. Since absorption involves the creation operator $e_\sigma^\dagger$ acting on the initial state, all contributions of the initial state where the local level is occupied are annihilated by the $e_\sigma^\dagger$-operator, and the initial density matrix ρ^i is projected onto a new one $\hat{\rho}_p^f = e_\sigma^\dagger \hat{\rho}^i e_\sigma (1 - \widetilde{n}_{e\sigma}^i)$. The factor $(1 - \widetilde{n}_{e\sigma}^i)$ is chosen to normalize the occupation at $t = 0$ to $\widetilde{n}_{e\sigma}(0) = 1$ so that the initial σ-occupation is 1, which is the case after an absorption process has taken place.

Charge $\widetilde{n}_e(t) = (\widetilde{n}_{e+} + \widetilde{n}_{e-})$ and magnetization $\widetilde{m}_e(t) = \frac{1}{2}(\widetilde{n}_{e+} - \widetilde{n}_{e-})$ are the two most important quantities characterizing the state of the quantum dot. Fig. 5.3 shows the non-equilibrium time evolution of these quantities, calculated with time-dependent NRG for $T = 0$. One can make out two distinct time scales. First, fluctuations of charge start at approximately $t \simeq 1/|\varepsilon_{e\sigma}^f|$. Second, the graph shows that charge fluctuations die out rather soon, but spin needs much longer to equilibrate, namely $t \simeq 1/T_K$. After this time, the so called Kondo cloud has built up, which screens the local spin into a singlet by electrons hopping to and away from the dot. The spin-equilibration is mediated by electrons tunneling between the local level and the FR. Thereby spin-flips are possible, as described in section 2.2. Since information between two e-level spin-flips is maintained, the dynamics of the

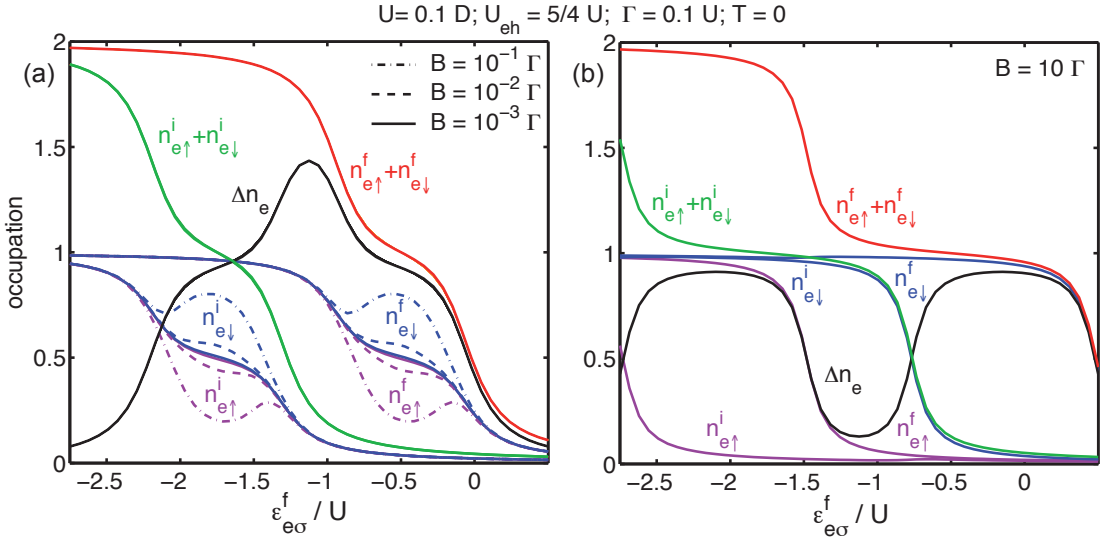

Figure 5.2: Occupation of the QD in the presence of an applied magnetic field.(a) The $\sigma =\uparrow$- and $\sigma =\downarrow$-population is shown by the blue and purple lines for three different magnetic fields (see figure legend). In the regions where the QD is in the LM-regime (initial or final state), the occupations of the spin-up and down-electrons become unequal as the B-field increases. However, the total occupation stays the same. (b) When B becomes $\gtrsim \Gamma$ the Zeeman-splitting of the two levels becomes larger than Γ and tunneling between the upper of the split levels and the FR is suppressed. Thus, the local moment regime, characterized by equal occupations of 1/2 for both spin directions of the local level, ceases to exist.

quantum dot are non-Markovian.

The values of $\widetilde{n}_{e\sigma}(t)$ and $\widetilde{m}_e(t)$ in the long time limit deviate from their known values by around 3%. This is an artifact of time-dependent NRG, which presumably occurs due to the fact that the resolution of the NRG-discretization scheme has rather coarse resolution at higher energies [22].

For larger temperatures, $T > T_K$, spin decays faster. For $T \neq 0$, $\widetilde{m}_e(t)$ equilibrates at $min\{\tau_{Kor}, 1/T_K\}$, with the Korringa relaxation time $\tau_{Kor} = ln^2(T/T_K)/T$ [7] (see Fig. 5.4).

5.3 Absorption lineshape

The analysis of the absorption lineshape is the central goal of this thesis. Absorption sets in as soon as a threshold frequency $\omega_{th} = E_G^f - E_G^i$ is exceeded, which is on the order of $\varepsilon_{e\sigma}^f + \varepsilon_{h\bar{\sigma}}$ (minus corrections from tunneling and correlations).

The absorption is calculated numerically according to Fermi's Golden Rule (see 4.26). For analytical purposes, Eq. (4.26) can be written as $A_\sigma(\nu) = -2\mathrm{Im}\mathcal{G}_{ee}^\sigma(\nu)$. For $T = 0$, $\mathcal{G}_{ee}^\sigma$ is then given by

$$\mathcal{G}_{ee}^\sigma(\nu) = {}_i\langle G|e_\sigma \frac{1}{\nu_+ - \bar{H}^f} e_\sigma^\dagger |G\rangle_i, \tag{5.1}$$

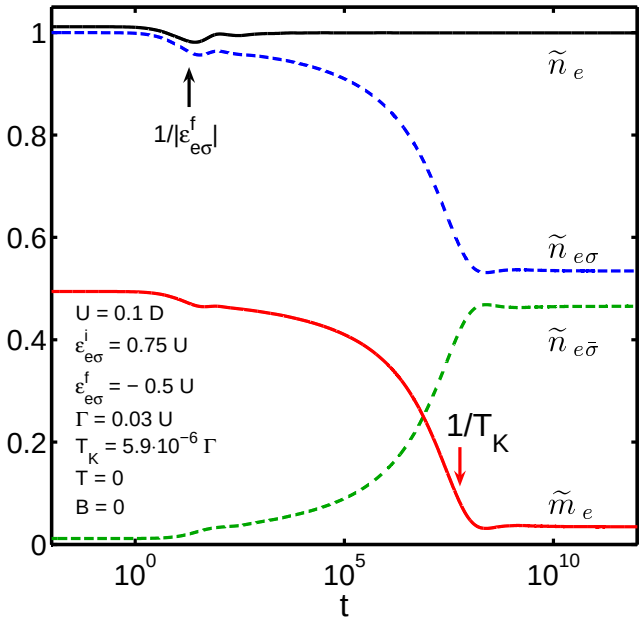

Figure 5.3: Non-equilibrium time evolution of charge and spin of the photo-excited electron for $T = 0$. The curves show the non-equilibrium time-evolution of spin and charge of the photo-excited electron after the creation of an $e^\dagger_+ h^\dagger_-$ exciton at $t = 0$. After the e-level's total charge $\widetilde{n}_e$ has equilibrated rather fast on a time scale of $1/|\varepsilon^f_\sigma|$, the equilibration of the spin-σ populations $\widetilde{n}_{e\sigma}(t)$ and magnetic moment of the local electron $\widetilde{m}_e(t)$ needs more time and happens on the time scale of $1/T_K$. The long-time limits $\widetilde{n}_{e\sigma}(\infty)$, $\widetilde{n}_{e\bar{\sigma}}(\infty)$ and $\widetilde{m}_e(\infty)$ deviate from their expected equilibrium values of 1, 1/2 and 0, respectively, by about 3 %. These artifacts emerge probably due to the discretization procedure needed for NRG, which is rather coarse for high energies.

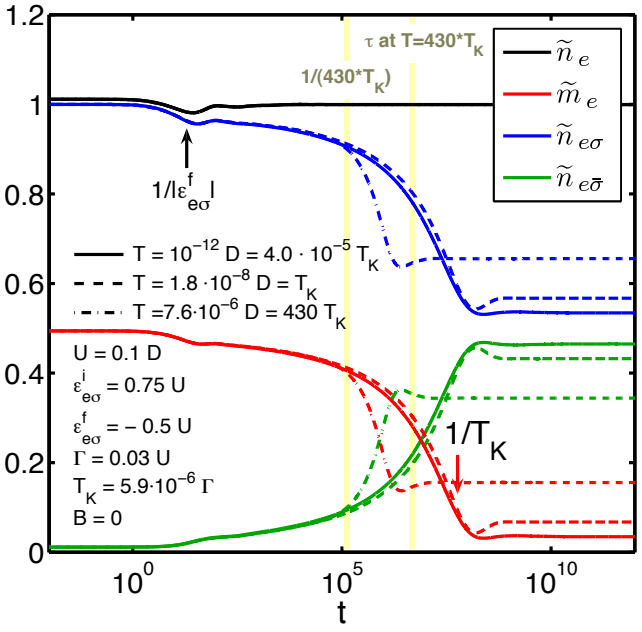

Figure 5.4: Non-equilibrium time evolution of spin and charge of the photo-excited electron for three different temperatures. Plotted is the time-evolution of spin and charge for the same parameters as in Fig. 5.3, but for three different temperatures $T \ll T_K$, $T = T_K$ and $T \gg T_K$, indicated by solid, dashed and dash-dotted lines, respectively. Charge-equilibration is independent of temperature and happens on a scale of $1/|\varepsilon^f_{e\sigma}|$. Equilibration of $\widetilde{m}_e$ depends on temperature only for $T > T_K$. In this case the spin gets already screened at the Korringa relaxation time τ_{Kor}.

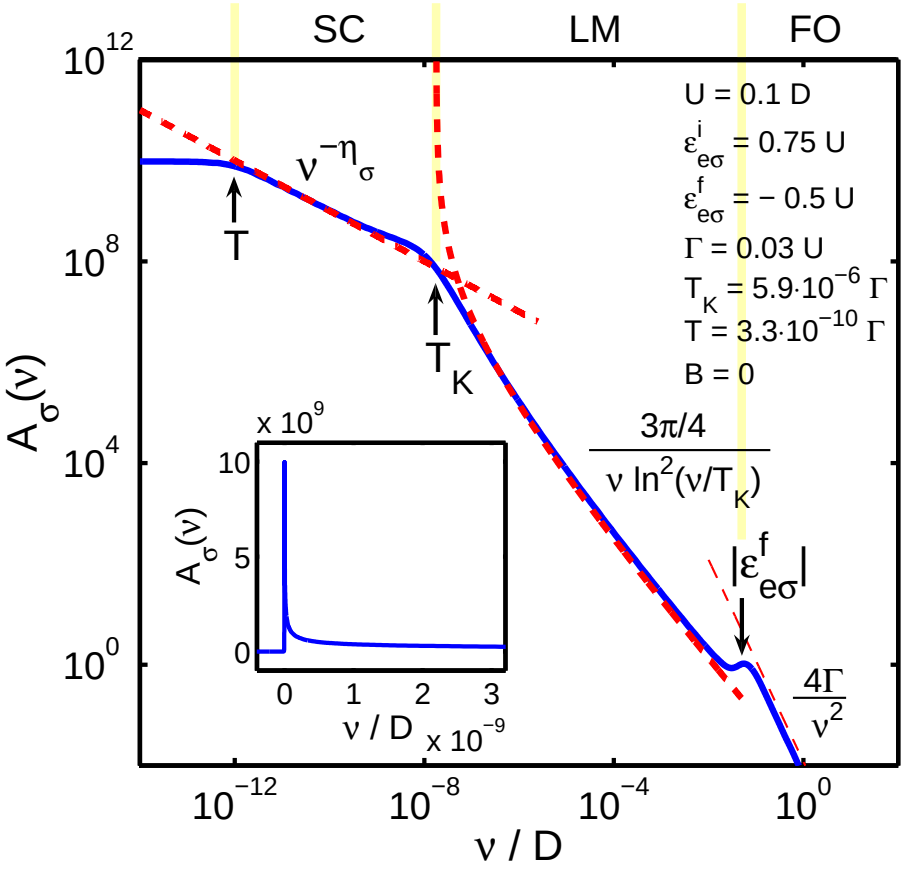

Figure 5.5: NRG vs. analytic results for the $B = 0$ absorption lineshape. The blue line shows the absorption spectrum calculated by NRG on a log-log plot, the inset on a linear plot. On a double-logarithmic scale, three distinct functional forms become visible, which can be described by analytic expressions (red dashed lines) for large, intermediate and small detuning. According to the fixed point perturbation theory these regions are identified and labelled with the common abbreviations, FO, LM, SC. Arrows and light yellow lines indicate the crossover scales T, T_K and $|\varepsilon^f_{e\sigma}|$.

where $\nu_+ = \nu + i0$ and $\bar{H}^f = H^f - E^i_G - \omega_{th}$. Its Fourier representation $\mathcal{G}^\sigma_{ee}(\nu) = \int \mathrm{d}t e^{it(\nu_+ + \omega_{th})} G^\sigma_{ee}(t)$ with $G^\sigma_{ee}(t) = -i\theta(t)_i\langle G|e^{iH^i t} e_\sigma e^{-iH^f t} e^\dagger_\sigma|G\rangle_i$ shows that this correlator probes the dynamics of an electron coupled to a FR after photon-absorption.

Eq. (4.26) can be evaluated with NRG. Fig. 5.5 shows an absorption spectrum for $T < T_K$ that exhibits all relevant features.

The inset shows the absorption spectrum on a linear scale. It reveals the threshold behavior of the absorption and and gives indication to a divergence near this threshold, which can be clearly seen on the main plot. The main panel shows the absorption lineshape on a log-log plot, where it is clearly visible that the spectrum can be divided in three different regimes that correspond to the fixed points of the Single Impurity Anderson Model (see 4.2): the Free Orbital regime (FO), the Local Moment regime (LM) and the Strong Coupling regime (SC). At the FO-regime, i. e. at high excitation energies, the electron has enough energy to give rise to tunnel

processes between the local level and the FR, so in this regime charge fluctuations can occur. In the LM-regime the electron does not have enough energy to make a real transition out of the dot, but virtual transitions into the reservoir and back are still possible. Thus, the quantum dot has a local moment and spin fluctuations can take place, a set-up which has the potential to show Kondo-physics. In the SC-regime the spin of the electron is totally screened and the combined system of electron and FR is in a Kondo-state.

These regimes can be approximated by the following analytical expressions which are derived in sections 5.3.1 to 5.3.3:

$$\text{(FO)} \quad |\varepsilon^{\mathrm{f}}_{\mathrm{e}\sigma}| \lesssim \nu \lesssim D \quad : \; A \propto \nu^{-2}\theta(\nu - |\varepsilon^{\mathrm{f}}_{\mathrm{e}\sigma}|) \; ; \tag{5.2a}$$

$$\text{(LM)} \quad T_{\mathrm{K}} \lesssim \nu \lesssim |\varepsilon^{\mathrm{f}}_{\mathrm{e}\sigma}| \quad : \; A \propto \nu^{-1} \ln^{-2}(\nu/T_{\mathrm{K}}); \tag{5.2b}$$

$$\text{(SC)} \quad T \lesssim \nu \lesssim T_{\mathrm{K}} \quad : \; A \propto \nu^{-\eta_\sigma} \; . \tag{5.2c}$$

5.3.1 Large Detuning

For large detuning, i. e., probing times $t \lesssim 1/|\varepsilon^f_{e\sigma}|$, the incident photon has enough energy for an electron to leave the e-level into the Fermi Sea or for an additional electron to occupy the e-level, coming from the FR. So for large detuning, the e-level appears as a free orbital, perturbed by charge fluctuations, which is a characteristic feature of the Free-Orbital regime.

The free orbital fixed point Hamiltonian $H^*_{FO} = H_c + H^f_{QD}$ can be used to describe this regime analytically. It consists of the Hamiltonian of the FR, H_c, and the Hamiltonian of the QD in the final state H^f_{QD}. The perturbation caused by charge fluctuations is given by the tunneling Hamiltonian H_t.

Fixed point perturbation theory for large detuning yields the following analytical expression for the absorption lineshape:

$$A^{FO}_\sigma(\nu) = \frac{4\Gamma}{\nu^2}\theta(\nu - |\varepsilon^f_{e\sigma}|), \tag{5.3}$$

The factor $\frac{4\Gamma}{\nu^2}$ has its origin in the charge fluctuations between e-level and FR. Both transitions from the valence-level into unfilled states of the FR and from the valence-level to a double occupied e-level contribute a factor of 2Γ. For such transitions the e-level is occupied in an intermediate state and the Lorentzian-broadening of the e-level due to charge fluctuations yields the functional dependence of ν^{-2}. The calculations that determine 4Γ as prefactor in Eq. (5.3) assume that the e-level is empty in the initial state. This assumption involves a certain approximation, since the initial occupation is in fact not zero but finite, due to finite tunneling. This causes the numerically calculated $A_\sigma(\nu)$ to be slightly lower than the analytically expected 4Γ. This can be seen in Fig. 5.5 where the lineshape in the FO-regime is slightly below the analytical expression. If absorption is calculated with $\Gamma^i = 0$ (see Fig. 5.6), Eq. (5.3) agrees with the numerical result completely.

The crossover to the LM-regime yields a small side peak in the absorption spectrum (see Fig. 5.7). (This is not surprising, since $A^{LM}_\sigma(|\varepsilon^f_{e\sigma}|) \neq A^{FO}_\sigma(|\varepsilon^f_{e\sigma}|)$ (see Eqs. (5.3), (5.4)). It is more pronounced for small Γ and smears out as hybridization increases.

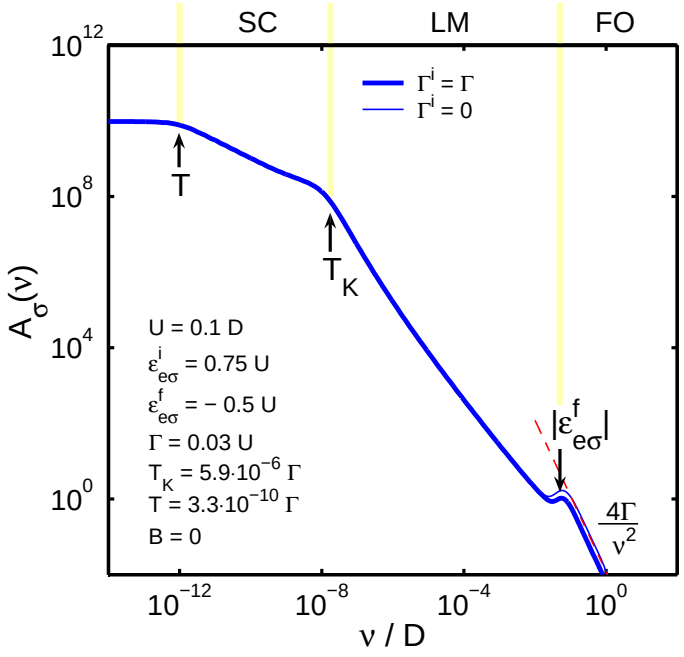

Figure 5.6: Absorption curves for vanishing and non-vanishing tunnel coupling of the initial Hamiltonian. The thick and thin lines show the absorption spectrum from Fig. 5.5, calculated for finite and zero Γ^i, respectively. The thick and thin lines mostly coincide, showing a small difference only in the FO-regime. $\Gamma^i = 0$ results in a totally unoccupied dot in the beginning, which makes both tunneling processes of the FO-regime (tunneling out of the local electron or tunneling onto the dot of an additional electron) equally possible and results in the analytical prefactor of $2 \cdot 2\Gamma = 4\Gamma$. Apart from the different prefactor in the FO-regime, the lineshapes for $\Gamma^i = \Gamma$ and $\Gamma^i = 0$ show no difference.

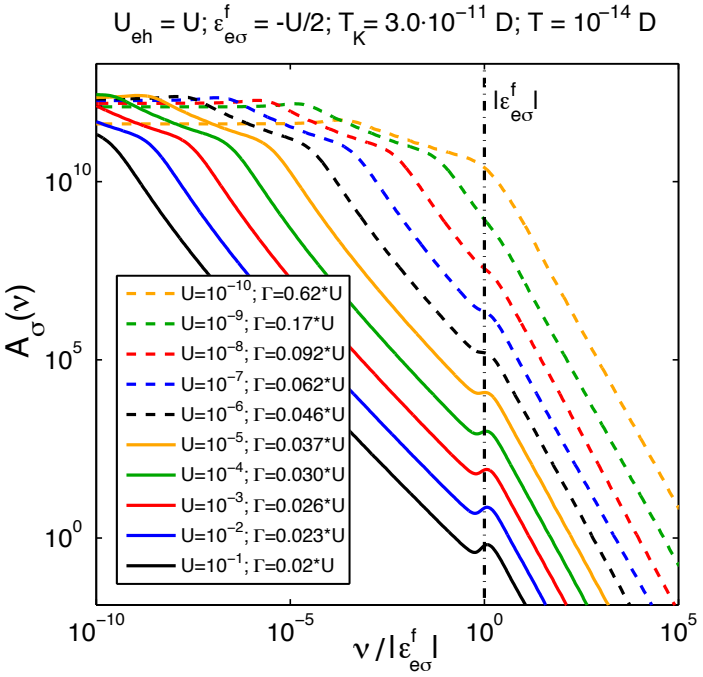

Figure 5.7: Emergence of the side peak at the LM-FO crossover as Γ is gradually reduced. We chose to decrease Γ and U in a way that keeps the absolute value of T_K constant, which makes the lineshapes easy to compare. The side peak that marks the crossover between large and intermediate detuning becomes more pronounced as Γ is decreased with respect to U. For frequencies above $|\varepsilon^f_{e\sigma}|$ the photon has enough energy for an electron to tunnel out or onto the dot. At this crossover suddenly new absorption processes become possible, which result in different $A_\sigma(\nu)$ and give rise to a small peak.

5.3.2 Intermediate Detuning

For intermediate detuning, $T_K < \nu < 1/|\varepsilon^f_{e\sigma}|$, that probes times $1/|\varepsilon^f_{e\sigma}| \lesssim t \lesssim 1/T_K$, the photon does not have enough energy to cause real charge fluctuations. However, virtual charge fluctuations are still possible, which give rise to spin fluctuations of the local moment (see 2.2) [20],[18]. This regime can be described analytically by perturbation theory using the fixed point Hamiltonian of the Local Moment regime $H^*_{LM} = H_c + const.$. The perturbation is given by a Kondo term, that causes spin fluctuations: $H'_{LM} = \frac{J}{\rho}\vec{s}_e \cdot \vec{s}_c$, where $\vec{s}_j = \frac{1}{2}\sum_{\sigma\sigma'} j^\dagger_\sigma \vec{\tau}_{\sigma\sigma'} j_{\sigma'}$ $(j = e, c)$ are the spin-operators for the local level and the Fermi Reservoir, $\vec{\tau}$ are the Pauli matrices and $J = 2U\Gamma/|\pi\varepsilon^f_e(\varepsilon^f_e + U)|$ is an effective coupling constant [16].

Carrying out fixed point perturbation theory yields the following analytical expression for $A_\sigma(\nu)$ in the LM-regime:

$$A^{LM}_\sigma(\nu) = \frac{3\pi}{4}\frac{J^2(\nu)}{\nu}, \tag{5.4}$$

where $J(\nu) = \ln^{-1}(\nu/\mathrm{T_K})$ is the renormalized, scale-dependent exchange constant, that arises from scaling arguments [16]. The agreement between analytical and numerical results can be seen in Fig. 5.5.

For intermediate detuning, the absorption lineshape depends on $\varepsilon^f_{e\sigma}$ and U only indirectly via T_K, which makes it a universal function of ν and T_K, as can be seen in Fig. 5.8. The lower left inset shows the lineshapes for five different values of $\varepsilon^f_{e\sigma}$ which lie symmetrically around $-U/2$, and accordingly for three different values of T_K (see upper inset). Plotting the rescaled lineshapes $A_\sigma(\nu)/A_\sigma(T_K)$ vs. ν/T_K shows that they collapse onto a universal scaling curve within the LM regime $T_K \lesssim \nu \lesssim |\varepsilon^f_{e\sigma}|$ (main plot).

5.3.3 Small Detuning

For low frequencies, which are below T_K, the frequency dependent coupling constant $J(\nu)$ exceeds 1 and leads to the strong coupling regime. Here, the system can no longer be regarded as a Fermi-sea with a small perturbation, but one has to look at the system as a whole due to the strong interactions between dot-electron and reservoir. In this regime, which corresponds to long times $t > 1/T_K$, a screening cloud of electrons builds up, that screens the local moment, so that the dot exhibits a spin singlet.

The other electrons of the FR can now scatter off this singlet, which acts as a strong, static scattering site and which shifts the phase of an incident mode $k\sigma$ by $\delta_\sigma(\varepsilon_{k\sigma})$ with regard to its initial value. According to Nozières, the physics in this regime can be described by the strong coupling fixed-point Hamiltonian $H^*_{SC} + H'_{SC}$ (given explicitly in Appendix A.1). However, this Hamiltonian is defined solely by the phase-shifted electrons of the conduction band; the operators of the e-level, e and $e^\dagger$, do not show up in this Hamiltonian, since the c-electrons screen the local moment completely.

The fact that the Hamiltonian does not explicitly depend on the electrons of the e-level presents us with a problem: how is absorption to be described, which requires, a priori, reference to the operators e and $e^\dagger$? This problem can be solved

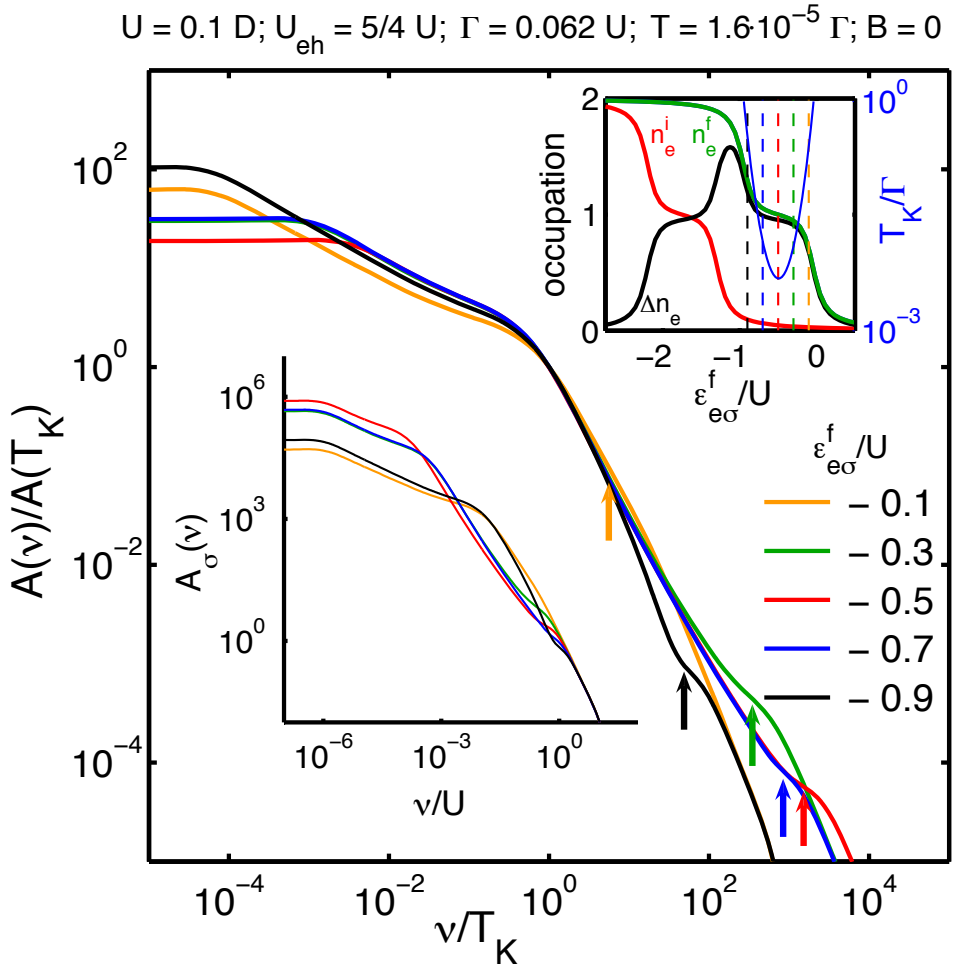

Figure 5.8: Universality in the LM-regime. The lower left inset shows the lineshapes for five different values of $\varepsilon^f_{e\sigma}$, indicated by colored arrows (main figure) or dashed lines (upper right inset). The main figure shows that the lineshapes collapse onto a universal curve in the LM-regime $T_K \lesssim \nu \lesssim |\varepsilon^f_{e\sigma}|$ when they are appropriately rescaled as indicated at the axis labels of the main figure. In the SC-regime, $T \lesssim \nu \lesssim T_K$, the exponent η_σ depends on $\varepsilon^f_{e\sigma}$ via Δn_e and thus the curves do not collapse here. The upper inset shows the occupations and Kondo temperatures depending on the position of the local level.

by using two tricks (described in detail in Appendix A.1): First, one works in the time-domain and performs a Fourier-Transformation at the end, and second, one uses equations of motion to relate the correlator for the local level, $G^{\sigma}_{ee}(t)$ to the correlator $G^{\sigma}_{cc}(t)$ (see A.1), which depends on FR electrons and is known from the X-ray edge problem. For the latter, an X-ray photon transfers an electron from an atomic core level to the conduction band instantaneously and creates a core hole, which acts as a local scattering potential, similar to the spin-singlet at a Kondo-state [26], [27], [28].

With the relation between $G^{\sigma}_{ee}(t)$ and $G^{\sigma}_{cc}(t)$, analytical calculations yield a power-law behavior for this regime:

$$A^{SC}_{\sigma}(\nu) \propto T_K^{-1}(\nu/T_K)^{-\eta_\sigma}. \tag{5.5}$$

The exponent η_σ depends on the change in average occupation of the e-level $\Delta n_{e\sigma} = \bar{n}^f_{e\sigma} - \bar{n}^i_{e\sigma}$ and can be expressed in three different ways, which will now be discussed:

$$\eta_\sigma = 2\Delta n_{e\sigma} - \sum_{\sigma'} (\Delta n_{e\sigma'})^2, \tag{5.6}$$

$$\eta_\sigma = 1 - \sum_{\sigma'} (\Delta n'_{e\sigma'})^2, \tag{5.7}$$

$$\eta_\sigma = \frac{1}{2} + 2m^f_e\sigma - 2(m^f_e)^2, \qquad \text{for } \bar{n}^i_e = 0, \bar{n}^f_e = 1. \tag{5.8}$$

Eq. (5.6) is a generalization of "Hopfield's rule of thumb" ($\eta = \Delta n - \frac{(\Delta n)^2}{2}$) [27], [29], [30] which is valid for vanishing magnetic field, where occupations are not spin dependent, i. e., $\Delta n_{e\sigma} = \Delta n_e/2$, so that the exponent is not spin dependent either.

In Eq. (5.7) $\Delta n'_{e\sigma'} = \Delta n_{e\sigma} - \delta_{\sigma\sigma'}$ is the charge difference of the local level between the ground state of the final Hamiltonian $|\infty\rangle$ (for $t \to \infty$) and the state which the system has right after absorption $|0^+\rangle$. In this form the second term of Eq. 5.7 can be identified with the contribution coming from Anderson orthogonality [31] between $|\infty\rangle$ and $|0^+\rangle$, which is part of the physics at this absorption process.

In Eq. (5.8) $m^f_e = \frac{1}{2}(\bar{n}^f_{e+} - \bar{n}^f_{e-})$ is the final magnetization, which is a universal function of g_eB/T_K. For $\bar{n}^i_e = 0$ and $\bar{n}^f_e = 1$, the exponents $\eta_\sigma(B)$ are therefore universal functions of g_eB/T_K, too (see Fig. 5.9b).

With finite magnetic field, absorption becomes spin-dependent. This can be easily seen for high magnetic fields, $|B| \gg T_K$, where $\Delta n_{e,lower} \to 1$ and $\Delta n_{e,upper} \to 0$, so that the exponents η_σ reach the following limits (Fig. 5.9a):

$$\eta_{lower/upper} \to \begin{cases} \frac{1}{2} & (|B| \ll T_{\mathrm{K}}) \,, \\ \pm 1 & (|B| \gg T_{\mathrm{K}}) \,. \end{cases} \tag{5.9}$$

In Eq. (5.9) the subscript "lower" or "upper" indicates whether the electron is excited to the lower or upper Zeeman-split e-level, which is determined by polarization of the incident photon. For $|B| \gg T_K$, η_{lower} and η_{upper} show different signs because the change in local charge becomes asymmetric ($\Delta n_{e,lower} \to 1$ whereas $\Delta n_{e,upper} \to 0$ (see Fig. 5.2)). As a consequence for $\sigma =$ lower, there is no Anderson orthogonality

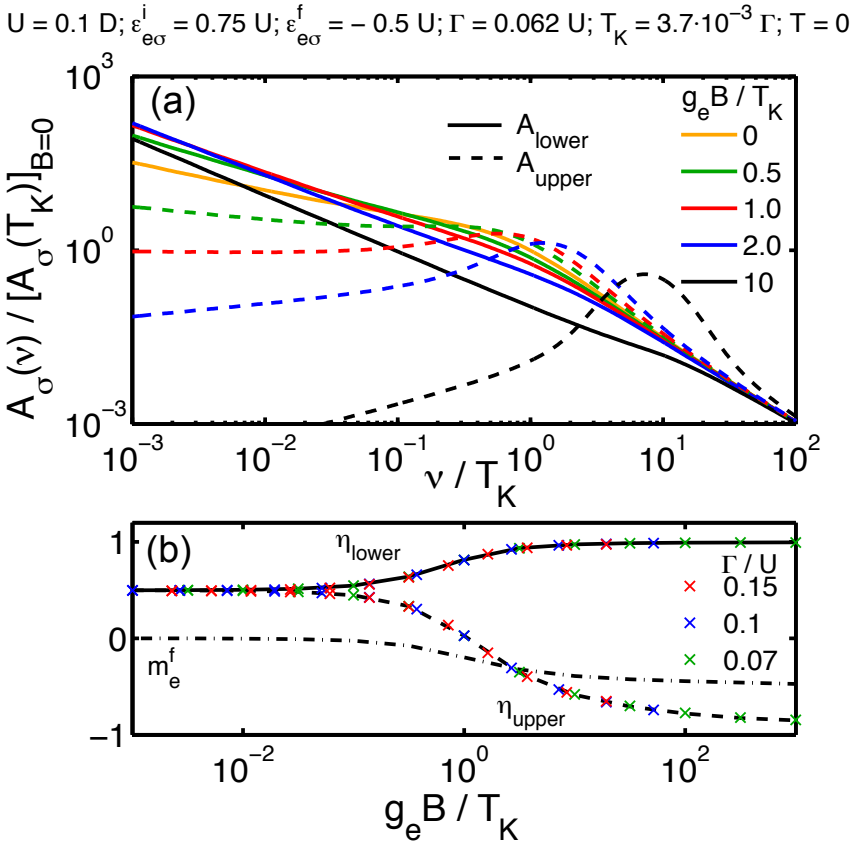

Figure 5.9: Magnetic-field dependence of lineshape. (a) The magnetic field causes a split of the local level. Depending on whether the electron is excited to the lower or upper of these levels (indicated by solid or dashed lines, respectively) the divergence at the threshold-frequency is either amplified or suppressed. (b) Universal dependence of the magnetization m_e^f and the infrared exponents η_{lower} (solid line) and η_{upper} (dashed line) on g_eB/T_K. η_σ is extracted from the absorption lineshape $A_\sigma(\nu)$ for several different magnetic fields and three values of Γ

($\Delta n'_{e\sigma'} = 0$) while for $\sigma =$ upper it becomes maximal ($\Delta n'_{e\sigma'} = 1$). The conclusion is that a magnetic field can tune the strength of the Anderson orthogonality, thus causing a spin-dependence of the lineshape $A(\nu) \propto \nu^{-\eta_\sigma}$, which becomes more pronounced with increasing $|B|$, finally leading to the limits of Eq. (5.9). This means that while for $A_{lower}(\nu)$ the near-threshold singularity is strengthened towards ν^{-1}, for $A_{upper}(\nu)$ it changes towards ν^{+1}. The latter is a power-law decay with decreasing ν (instead of a singularity) and has its absorption maximum near $\nu = |g_eB|$ (see Fig. 5.9) which can be associated with the transition into the upper Zeeman-split e-level.

Hopfield's rule of thumb is valid for a wide range of $|\varepsilon_e^f|$ and B. How well Hopfield's rule agrees with the absorption spectrum can be seen in Fig. 5.10. The solid lines were calculated with Eq. (5.6), where $\Delta n_{e\sigma}$ was calculated with NRG. The triangles show exponents η_σ that were directly extracted from power-law fits to the low-frequency regime of the absorption spectrum.

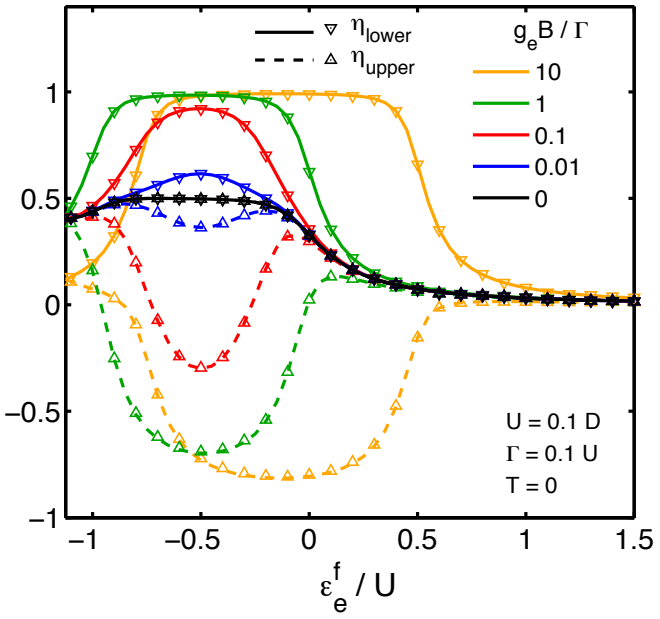

Figure 5.10: Checking Eq. (5.6) Hopfield's rule of thumb for the singularity exponent η_σ for various combinations of $|\varepsilon_e^f|$ and B. The values forming the solid and dashed lines were calculated with the r. h. s. of Eq. (5.6) where $\Delta n_{e\sigma}$ was calculated with NRG. The triangular symbols show the values of η_σ extracted from power-law fits to the low-frequency regime of $A_\sigma(\nu)$. The two calculation methods yield the same values for η_σ within 1%

5.3.4 Temperature dependence

The NRG results presented in the previous sections were all calculated for a finite, albeit very small, temperature T. This is a generalization to [32] where $T = 0$ was assumed. The behavior of the absorption spectrum as temperature is increased is shown in Fig. 5.11.

There, temperature is successively reduced, which leads to a strong asymmetry of the lineshape and to an extreme increase in peak height. This behavior of the lineshape can be understood by looking at the loglog-plot. One has to distinguish whether temperature is above or below T_K.

$T < T_K$: Fig. 5.5 shows a loglog-plot of the absorption spectrum for $T < T_K$. Here, temperature simply cuts off the divergence for $\nu < T$, leading to very high absorption near the threshold for $T \to 0$. For $\nu > T$ the absorption spectrum does not depend on temperature and can be divided into the three regimes discussed above.

$T > T_K$: For the calculation of $A_\sigma(\nu)$ one has to set $H^f \to H_r^* + H_r'$ in Eq. (5.1) and expand in powers of H_r' for r = FO or LM. The generalization of Eq. (5.1) for finite T is $\mathcal{G}_{ee}^\sigma(\nu) = \mathcal{F}_\nu\{-i\theta(t)\langle e_\sigma(t)e_\sigma^\dagger\rangle_i\}$. Here, we give only the lineshape for

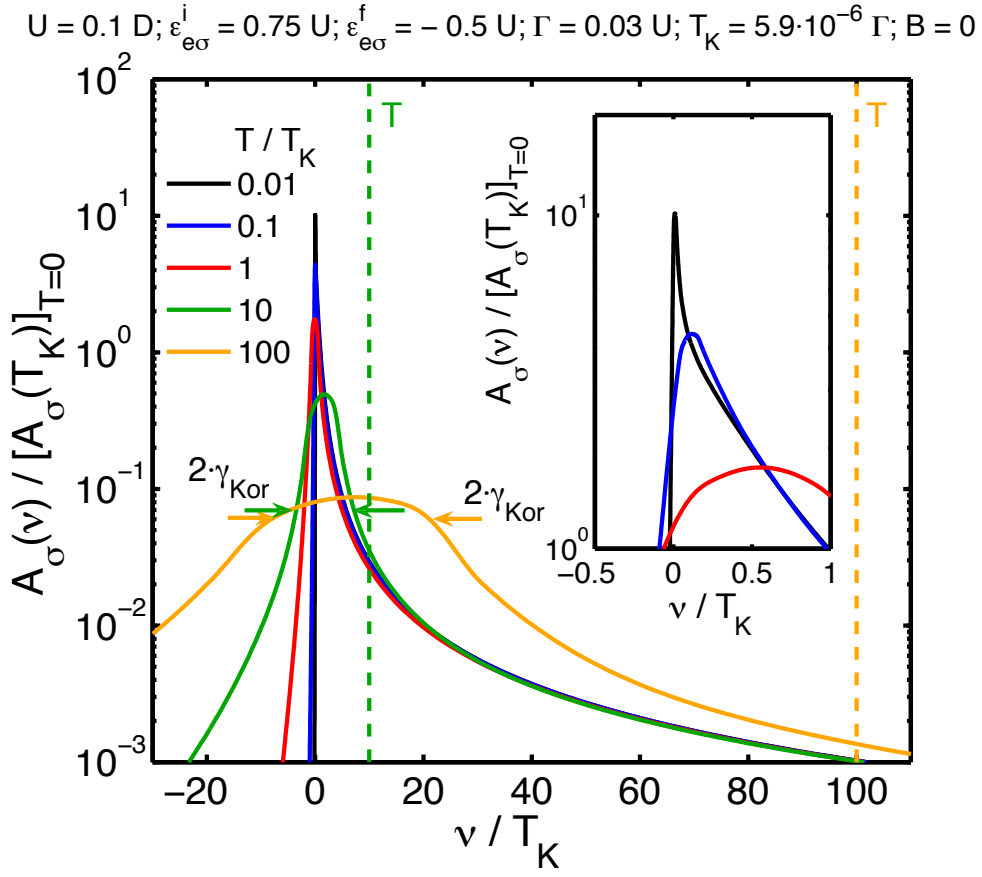

Figure 5.11: Absorption lineshape calculated for several different temperatures shown on a semi-log plot. For $T < T_K$ the near-threshold divergence is cut off at $\nu = T$ and the lineshape changes only slightly. For $T > T_K$ there is still a pronounced peak in the absorption line for small detuning, whose width is on the scale of the Korringa relaxation rate γ_{Kor}, which is significantly lower than temperature. The inset shows a blow-up of the absorption peaks and shows how the lineshapes differ for $T \lesssim T_K$.

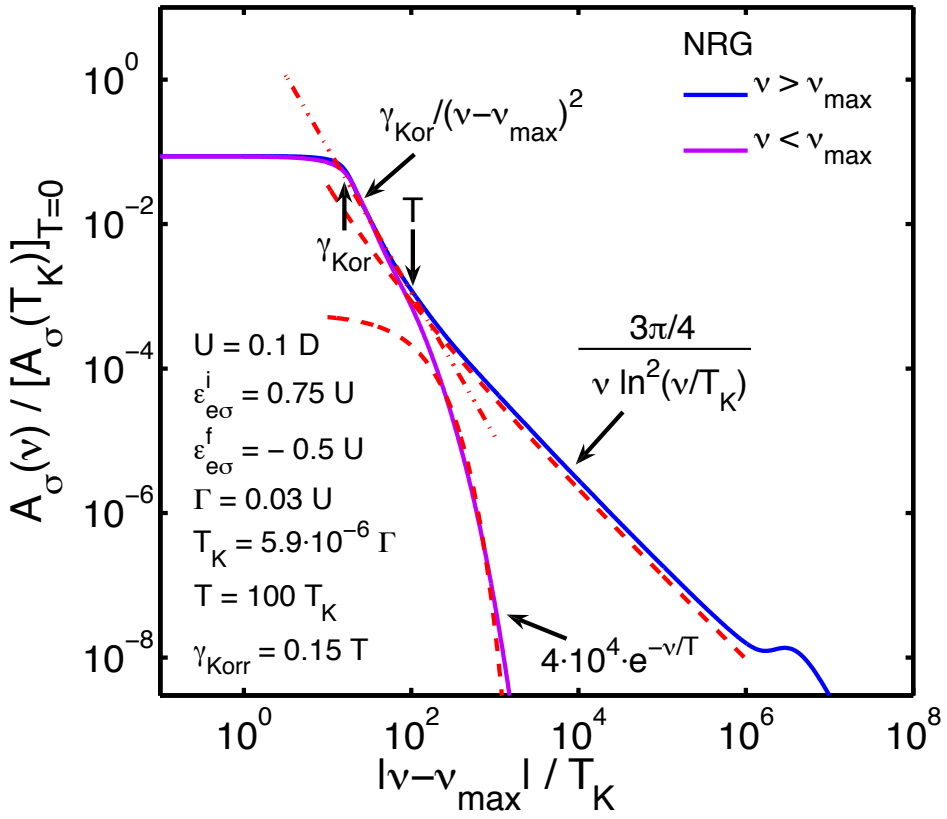

Figure 5.12: Absorption lineshape at large temperature $T \gg T_K$. The plot shows the red-detuned ($\nu < \nu_{max}$) and the blue-detuned ($\nu > \nu_{max}$) part of the absorption lineshape. ν_{max} is the frequency where $A_\sigma(\nu)$ has its maximal value. For $\nu - \nu_{max} > T$ the lineshape does not depend on temperature. For $\nu - \nu_{max} < T$ absorption still increases for frequencies below T, as long as $(\nu - \nu_{max}) \lesssim \gamma_{Kor}$. For red-detuning ($\nu < \nu_{max}$), absorption is possible from thermally excited initial states which results in an exponential behavior of the lineshape.

$|\nu| < |\epsilon^f_{e\sigma}|$:

$$A_\sigma(\nu) = \frac{3\pi/4}{1 - e^{-\nu/T}} \frac{\gamma_{Kor}(\nu, T)/\pi}{\nu^2 + \gamma^2_{Kor}(\nu, T)}, \tag{5.10}$$

where $\gamma_{Kor}(\nu, T)$ is the scale-dependent Korringa relaxation rate:

$$\gamma_{Kor}(\nu, T) = \begin{cases} \pi T / \ln^2 |T/T_K| & \text{for } |\nu| < T, \\ \pi \nu / \ln^2 |\nu/T_K| & \text{for } |\nu| > T. \end{cases} \tag{5.11}$$

For $\nu \gg T$, $A_\sigma(\nu)$ becomes equal to the expression for $T = 0$, given in Eq. (5.4).

5.3.5 Threshold frequency

The threshold behavior of the absorption spectrum can be clearly seen on a linear scale, as shown in the inset of Fig. 5.5. The threshold frequency is given by the

difference of the ground state energies of the final and initial Hamiltonian: $\omega_{th} = E_G^f - E_G^i$. Magnetic field influences the dot both via the energy level of the hole and via the ground-state energy of the system consisting of e-level and Fermi Reservoir. The change of threshold frequency with magnetic field is therefore given by $\omega_{th}(B) - \omega_{th}(0) = \frac{3}{2}\bar{\sigma} g_h B + \delta\omega_{th}^e(B)$, where the first term describes the Zeeman energy of the photo-excited hole with a pseudo-spin 3/2 (see 3 for further information) and the second term the B-dependence of the ground-state energy of the electron system. Due to the thermodynamic relation $g_e m_e^a = \partial E_G^a / \partial B$ one can measure the difference between the initial and final local moment in the ground states by combining all three equations to:

$$\partial(\delta\omega_{th}^e)/\partial B = g_e[m_e^f(B) - m_e^i(B)]. \tag{5.12}$$

For $\bar{n}_e^i \simeq 0$ and $\bar{n}_e^f \simeq 1$, Eq. (5.8) is valid and one gets a direct relation between the shift of threshold frequency and infrared singularity exponent.

From the asymptotic behavior of m_e^f for small and large fields, $m_e^f = -g_e B\chi_0 = -g_e B/4T_K$ and $|m_e^f| = \frac{1}{2}$, respectively, one obtains the asymptotic behavior for the change of threshold frequency:

$$\delta\omega_{\mathrm{th}}^{\mathrm{e}} = \begin{cases} -(g_{\mathrm{e}}B)^2/8T_{\mathrm{K}} & (|B| \ll T_{\mathrm{K}}) \,, \\ -g_{\mathrm{e}}B/2 & (T_{\mathrm{K}} \ll B \ll |\varepsilon_{\mathrm{e}}^{\mathrm{f}}|) \,. \end{cases} \tag{5.13}$$

The formula $\delta\omega_{th}^e = T_K - \frac{1}{2}\sqrt{(g_e B)^2 + (2T_K^2)}$ gives an interpolation between these two asymptotical expressions, and, up to numerical prefactors, has the same form as the formula derived for the ground state energy of the s-d model in [33].

For small fields, one can use the fact that $\delta\omega_{th}^e$ depends on the Kondo temperature quadratically to determine it in the experiment. This is especially useful since ground state energy and magnetization of the local level are quantities that can only be determined with optical measurements, not with transport experiments.

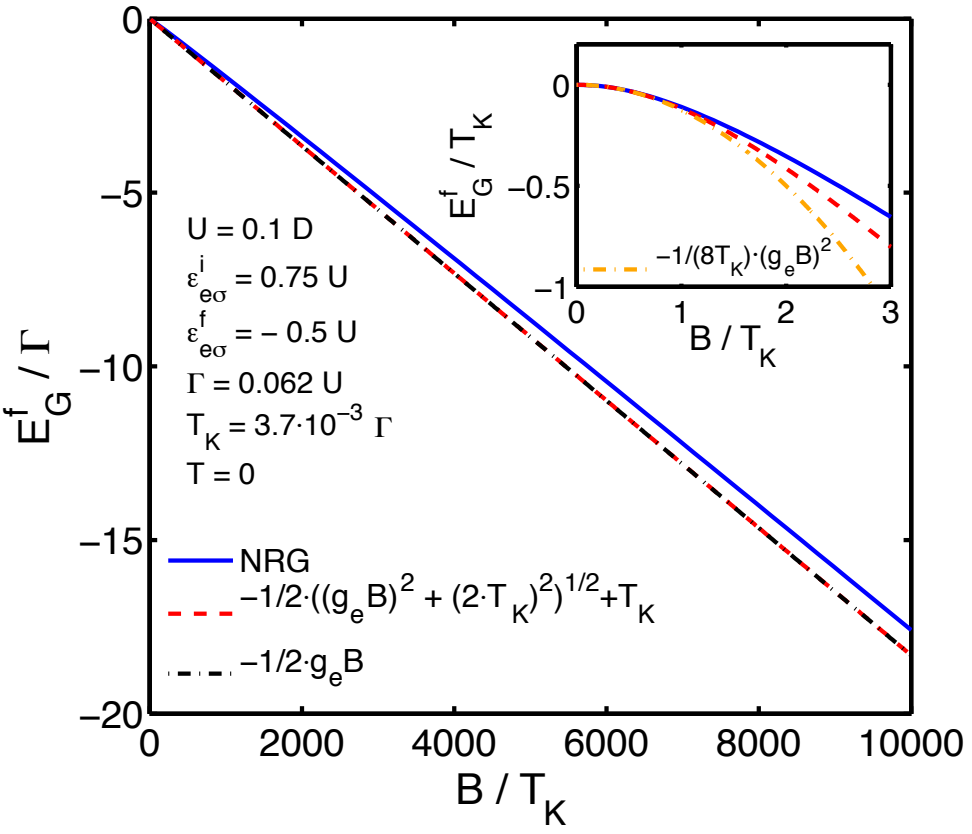

Figure 5.13: Dependence of the ground state energy on magnetic field. The blue line shows the ground state energy of the final Hamiltonian, E_G^f, plotted vs. B/T_K. The red line shows the analytic expression for E_G^f which is given by Eq. (5.13). Because of the hybridization of the e-level with the FR, the behavior of the ground state energy for high fields differs from $-\frac{1}{2}g_eB$. The inset shows that the behavior of the ground state energy is quadratic for small magnetic fields below T_K.

Chapter 6

Conclusions

The main aim of this thesis was to calculate the absorption spectrum of a quantum dot. This was done using an extension of the Anderson Model with two different Hamiltonians describing the dot before and after absorption, where the final Hamiltonian has a lower e-level due to the excitonic Coulomb attraction. This model was then used to calculate the absorption spectrum with the NRG-method, yielding the main result that the absorption lineshape can be divided in three different frequency regimes that correspond to the fixed points of the Single Impurity Anderson Model. Further, the influence of magnetic field on the spectrum was examined and it was shown that the exponent describing the power-law behavior of the lineshape at small detuning is related to the change of occupation at an absorption process and can be calculated by a generalization of Hopfield's rule. It turned out that the shape of the absorption line depends strongly on polarization for high magnetic fields. The absorption spectrum with its different frequency regimes was related to the time evolution of charge and spin where the time scales of equilibration correspond to the inverse frequency of the different frequency regimes.

For future work, it would be interesting to include further effects in the calculations that brings the theoretical work even closer to the experiment. This is especially interesting since optical signatures of Kondo Excitons are object of current research and more detailed calculations would make it easier to compare theory with experiment. Such additional effects could be for example Fano-effects, where the electron can directly reach the reservoir at absorption without occupying the local level in an intermediate state. Another aspect that would be interesting, is to further examine the time evolution of charge and spin and e. g. to determine not only time scales of equilibration but also the functional behavior. Although time-resolved measurements of how the Kondo-cloud builds up are not possible with current technology, they might be in the future, and apart from that, such calculations would give deeper understanding of the Kondo effect, from a point of view that was not taken before.

Appendix A

Appendix

A.1 Evaluation of the absorption lineshape in the strong-coupling-regime

For detunings far below the Kondo scale, $\nu \ll T_K$, the physics is governed by the strong coupling fixed point. It describes a fully screened singlet which is source of strong potential scattering for other FR electrons and causes the phase of each mode $k\sigma$ to shift by $\delta_\sigma(\varepsilon_{k\sigma})$ relative to its value for $H^{\rm i}$. According to Nozières [34] (see also [7]), the fixed point Hamiltonian at $B = 0$ is $H^*_{\rm SC} = \sum_{k\sigma} \varepsilon_k \tilde{c}^\dagger_{k\sigma} \tilde{c}_{k\sigma}$, where tildes mark operators representing phase-shifted modes. The leading relevant perturbation for $0 < B \lesssim T_{\rm K}$ has the form [34], [7] $H'_{\rm SC} = \sum_\sigma \sigma g_{\rm e} B \, [\, \sum_k \frac{1}{2} \tilde{c}^\dagger_{k\sigma} \tilde{c}_{k\sigma} + \tilde{\rho}_\sigma / (\pi \rho T_{\rm K}) \,]$.

This fixed point Hamiltonian cannot be directly used since the method of perturbing around the fixed point does not work for calculating $\mathcal{G}^\sigma_{\rm ee}(\nu)$ of Eq. (5.1). The reason is that $\mathcal{G}^\sigma_{\rm ee}(\nu)$ is formulated in terms of $e_{{\rm e}\sigma}$ and $e^\dagger_{{\rm e}\sigma}$ operators, whose dynamics is determined by higher-energy excitations of the FR which are *not* described by $H^*_{\rm SC} + H'_{\rm SC}$. This problem can be avoided by an equation of motion approach to first derive an asymptotic relation between the impurity Green's function and the Green's function of the reservoir-electrons.

First, it is important to note that the correlator occurring in Eq. (5.1) can be expressed as the Fourier transform, $\mathcal{G}^\sigma_{\rm ee}(\nu) = \mathcal{F}_\nu \{G^\sigma_{\rm ee}(t)\}$, of the correlator

$$G^\sigma_{\rm ee}(t) \;=\; -i\theta(t) \, \langle e_\sigma(t) e^\dagger_\sigma \rangle_{\rm i} \; , \tag{A.1}$$

which involves operators defined to have an anomalous time dependence with both $H^{\rm i}$ and $H^{\rm f}$: $\hat{O}(t) = e^{iH^{\rm i}t} \hat{O} e^{-iH^{\rm f}t}$. This dependence arises from suddenly lowering the e-level.

To relate $\mathcal{G}^\sigma_{\rm ee}(\nu)$ to a similarly-defined correlator $\mathcal{G}^\sigma_{\rm cc}(\nu)$, it is important to note that the anomalous time-dependence of $c_{k\sigma}(t)$ leads to the equation of motion

$$\begin{aligned} i\partial_t c_{k\sigma}(t) \;&=\; [c_{k\sigma}(t), H^{\rm i}] + c_{k\sigma}(t)(\varepsilon_{{\rm h}\bar{\sigma}} - U_{\rm eh} n_{\rm e}) \; , & \text{(A.2)} \\ &=\; c_{k\sigma}(t)[\varepsilon_{k\sigma} + \varepsilon_{{\rm h}\bar{\sigma}} - U_{\rm eh} n_{\rm e}] + v e_\sigma(t) \; , & \text{(A.3)} \end{aligned}$$

where $v = \sqrt{\Gamma/\pi\rho}$. Inserting this into the definition of $G^\sigma_{kk'}(t)$ one finds

$$i\partial_t G^\sigma_{kk'}(t) \sim [\varepsilon_{k\sigma} + \varepsilon_{{\rm h}\bar{\sigma}}] G^\sigma_{kk'}(t) + v G^\sigma_{{\rm e}k'}(t) \; , \tag{A.4}$$

where terms that become subleading for $t \to \infty$ have been dropped (a term containing $\delta(t)$; and one containing $\langle c_{k\sigma}(t) n_{\rm e} c^\dagger_{k'\sigma}\rangle_{\rm i}$ which contains more operators and hence decays more quickly with time than the correlators that were retained). Similarly one finds

$$i\partial_t G^\sigma_{{\rm e}k'}(t) \sim [\varepsilon_{k'\sigma} + \varepsilon_{{\rm h}\bar{\sigma}}] G^\sigma_{{\rm e}k'}(t) + v G^\sigma_{\rm ee}(t) \; , \tag{A.5}$$

where the cyclic property of the trace was used to write

$$\langle [c_{{\rm e}\sigma}(t), H^{\rm i}] c^\dagger_{k'\sigma}\rangle_{\rm i} \;\; = \;\; \langle c_{{\rm e}\sigma}(t) [H^{\rm i}, c^\dagger_{k'\sigma}]\rangle_{\rm i} \; . \tag{A.6}$$

Fourier-transforming Eqs.(A.5) and (A.4) using the convention stated just before Eq. (A.1) and eliminating $\mathcal{G}^\sigma_{{\rm e}k'}(\nu)$, one finds the asymptotic relation:

$$\mathcal{G}^\sigma_{kk'}(\nu) \sim \frac{v^2 \mathcal{G}^\sigma_{\rm ee}(\nu)}{(\nu_+ + \Delta - \varepsilon_{k\sigma})(\nu_+ + \Delta - \varepsilon_{k'\sigma})} \; , \tag{A.7}$$

with $\Delta = \omega_{\rm th} - \varepsilon_{{\rm h}\bar{\sigma}}$. This leads to

$$\mathcal{G}^\sigma_{\rm cc}(\nu) = \sum_{kk'} \mathcal{G}^\sigma_{kk'}(\nu) \sim -\pi\rho\Gamma \mathcal{G}^\sigma_{\rm ee}(\nu) \; , \tag{A.8}$$

where the double sum $\sum_{kk'} = \rho^2 \int {\rm d}\epsilon_k {\rm d}\epsilon_{k'}$ is exhausted by two δ-functions, since $|\Delta|$ is of order $|\varepsilon^{\rm f}_{{\rm e}\sigma}|$, which is assumed to be smaller than the bandwidth D. Eq. (A.8) implies

$$A^{\rm SC}_\sigma(\nu) \sim \frac{2}{\pi\rho\Gamma} {\rm Im} \mathcal{G}^\sigma_{\rm cc}(\nu) \; . \tag{A.9}$$

To calculate $G^\sigma_{\rm cc}(t)$ for $t \gg 1/T_{\rm K}$, the replacements $H^{\rm i} \to H_{\rm c}$ and $H^{\rm f} \to H^*_{\rm SC} + H'_{\rm SC}$ can be made in Eq. (A.9):

$$G^\sigma_{\rm cc}(t) \sim {}_{\rm i}\langle {\rm G}| {\rm e}^{iH_{\rm c}t} c_\sigma {\rm e}^{-iH^*_{\rm SC}t} c^\dagger_\sigma |{\rm G}\rangle_{\rm i} \; . \tag{A.10}$$

This response function is similar to the one at the X-ray edge problem [26],[27],[28]: there absorption of an X-ray photon excites an atomic core electron into the conduction band (described by $c^\dagger_\sigma$), leaving behind a core hole that acts as a scattering potential with respect to $H_{\rm c}$ (described by $H^*_{\rm SC}$). The calculation of Eq. (A.10) (e.g. [28]) yields in leading power law

$$G^\sigma_{\rm cc}(t) \;\; \sim \;\; t^{-[(\delta_\sigma - \pi)^2 + \delta^2_\sigma]/\pi^2} \; . \tag{A.11}$$

where $\delta_\sigma = \delta_\sigma(0)$ denotes the phase shifts at the Fermi energy. There is an instructive interpretation for this power-law due to Hopfield [29]: according to Anderson's orthogonality catastrophe [31], two Fermi seas with different local scattering potentials that cause their modes to differ in phase by $\delta_\sigma(\varepsilon_{k\sigma})$, have a ground state overlap ${}_{\rm f}\langle G|G\rangle_{\rm i} \sim L^{-\sum_\sigma \delta^2_\sigma(0)/\pi^2}$ which vanishes in the limit of large system size $L \to \infty$. In analogy, Eq. (A.11) can be seen as the overlap ${}_{\rm f}\langle G|c^\dagger_\sigma|G\rangle_{\rm i}$ for systems of size $L \propto t$: the effect of $c^\dagger_\sigma$, which puts an extra spin-σ electron at the scattering site at $t = 0$, is similar to having an additional infinitely strong scatterer of σ-electrons in the initial,

but not in the final state, implying an extra shift $-\pi$ for the phase difference of the δ_σ modes.

The phase shifts at the Fermi energy, needed in Eq. (A.11), are given by $\delta_\sigma = \pi\Delta n_{\mathrm{e}\sigma}$, according to the Friedel sum rule [35], [36], valid for $T = 0$ and for arbitrary values of B, $\bar{n}_{\mathrm{e}}^{\mathrm{f}}$ and $\bar{n}_{\mathrm{e}}^{\mathrm{i}}$. Collecting results, one finds from Eqs. (A.9) and (A.11) that

$$A_\sigma^{\mathrm{SC}}(\nu) \sim {T_{\mathrm{K}}}^{-1}(\nu/T_{\mathrm{K}})^{-\eta_\sigma} \ , \tag{A.12}$$

where the infrared singularity exponent η_σ is given by Eq. (5.6),

$$\eta_\sigma = 2\Delta n_{\mathrm{e}\sigma} - \sum_{\sigma'} (\Delta n_{\mathrm{e}\sigma'})^2 \ . \tag{A.13}$$

The dimensionful prefactor in Eq. (A.12) was adjusted to make sure that Eqs. (A.12) and (5.2b) match, up to numerical prefactors, at the crossover scale $\nu = T_{\mathrm{K}}$, implying a prefactor $(\rho\Gamma){T_{\mathrm{K}}}^{\eta_\sigma - 1}$ in Eq. (A.11).

A.2 Bulk magnetic field

If a magnetic field is applied to the QD-setup, the electrons in the FR are affected by an energy shift of $\frac{1}{2} g_c B \sum_{k\sigma} c_{k\sigma}^\dagger c_{k\sigma}$. However, this influence was neglected throughout the calculations presented in the main text. The reason for this will be explained briefly. First, a bulk magnetic field polarizes the FR so that it exhibits a nonzero spin $\langle s_c^z \rangle \approx -\rho g_c B/2$. Thus the spin of the polarized FR can interact with the spin of the local level via the coupling term $\frac{J}{\rho} \vec{s}_c \vec{s}_e$. This adds a contribution of $-(J g_c/2) B s_e^z$ to the spin Hamiltonian of the local level and together with g_e it can be expressed as an effective local g-factor:

$$g_e^{eff} = g_e - g_c J/2 \tag{A.14}$$

Because J is the bare, not the renormalized exchange constant, its effect is rather small. This was checked with NRG as can be seen in Fig. A.2. There the dependence of the magnetization m_e^f on magnetic field is shown for several values for g_c and two different values for g_e. Although g_c has an effect on m_e^f for vanishing g_e, it is clearly visibly that this effect is negligible for non-vanishing g_e which was assumed throughout the thesis.

A.3 NRG parameters

Table A.1 lists the parameters that were used for the calculations of the figures in this thesis. For the calculation of the absorption spectra of Fig. 5.9 and Fig. 5.10, M_K was increased to avoid numerical artifacts. For the calculation of the QD-occupation and related quantities, the discrete data is summed up and no broadening is needed.

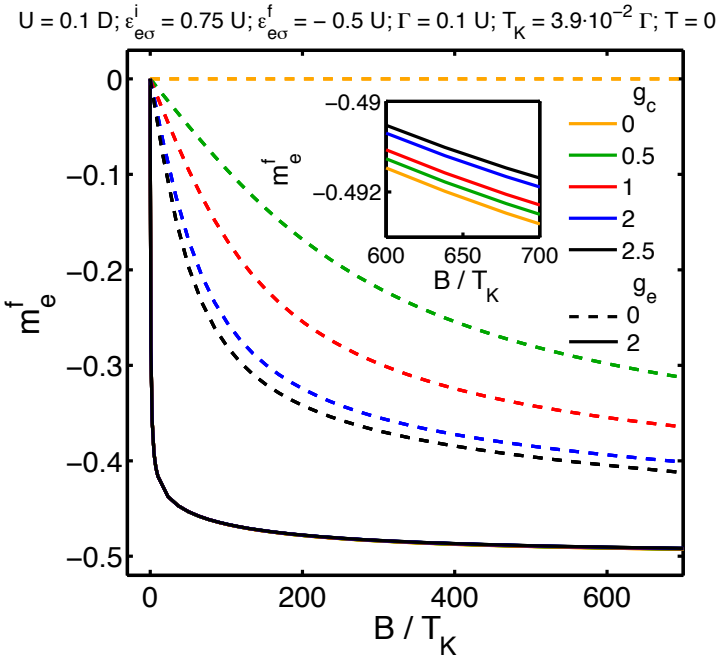

Figure A.1: Dependence of the magnetization on the g-factor of the leads g_c. The final magnetization m_e^f is plotted vs. B/T_K, for five different values of g_c, both with zero and nonzero g_e. If $g_e = 0$ (dashed lines), the magnetization depends on the value of g_c. Saturation of m_e^f occurs for B-fields much larger than T_K. If $g_e = 2$ (solid lines) the magnetization saturates at field-strengths around T_K, its dependence on g_c can be neglected and becomes visible only at high magnification (see inset).

Fig.	Λ	M_K	α
5.1	2.0	512	-
5.2	2.0	512	-
5.3	1.8	1024	0.4
5.4	1.8	1024	0.4
5.5	1.8	1024	0.5
5.6	1.8	1024	0.5
5.7	1.8	1024	0.4
5.8	1.8	1024	0.5
5.9	2.3	1200	0.6
5.10	2.3	1700	0.6
5.11	1.8	1024	0.4
5.12	1.8	1024	0.5
5.13	2.3	1024	-
A.1	2.3	1024	-

Table A.1: NRG-parameters for figures in the main part and the appendix. α is not required for the calculation of the QD-occupation and related quantities.

List of Figures

List of Tables

Bibliography

[1] L. Kouwenhoven and C. Marcus. *Quantum Dots.* Physics World **11**, 35-39 (1998)

[2] J. Kondo. *Resistance minimum in dilute magnetic alloys.* Progress of Theoretical Physics **32**, 37-49 (1964).

[3] W. J. de Haas, J. H. de Boer and G. J. van den Berg. *The electrical resistance of gold, copper and lead at low temperatures.* Physica (Utrecht) **1**, 1115 (1934).

[4] K. G. Wilson. *The renormalization group: Critical phenomena and the Kondo problem.* Rev. Mod. Phys. **47** 773-840 (1975).

[5] D. Goldhaber-Gordon, H. Shtrikman, D. Mahalu, D. Abusch-Magder, U. Meirav and M. A. Kastner. *Kondo effect in a single-electron transistor.* Nature **391**, 156-159 (1998).

[6] L. Kouwenhoven, L. Glazman. *Revival of the Kondo effect.* Physics World **14**, 33-38 (2001).

[7] L. Glazman and M. Pustilnik. *Nanophysics: Coherence and Transport*, edited by H. Bouchiat and et al. (Elsevier, Amsterdam, 2005), p. 427.

[8] W. G. van der Wiel, S. De Franceschi. *The Kondo Effect in the Unitary Limit.* Science **289**, 2105-2108 (2000)

[9] S. M. Cronenwett, T. H. Oosterkamp, L. P. Kouwenhoven. *A tunable Kondo effect in quantum dots.* Science **281**, 540-544 (1998).

[10] J. M. Smith, P. A. Dalgarno, R. J. Warburton, A. O. Govorov, K. Karrai, B. D. Gerardot and P. M. Petroff. *Voltage control of the spin dynamics of an exciton in a semiconductor quantum dot.* Phys. Rev. Lett. **94**, 197402 (2005).

[11] P. A. Dalgarno, M. Ediger, B. D. Gerardot, J. M. Smith, S. Seidl, M. Kroner, K. Karrai, P. M. Petroff, A. O. Govorov and R. J. Warburton. *Optically Induced Hybridization of a Quantum Dot State with a Filled Continuum.* Phys. Rev. Lett. **100**, 176801 (2008).

[12] A. O. Govorov, K. Karrai, and R. J. Warburton. *Kondo excitons in self-assembled quantum dots.* Phys. Rev. B **67**, 241307 (2003).

[13] O. Gunnarsson and K. Schönhammer. *Electron spectroscopies for Ce compounds in the impurity model.* Phys. Rev. B, **28**, 4315 (1983).

[14] P. W. Anderson. *Localized Magnetic States in Metals.* Phys. Rev. **124**, 41-53 (1961)

[15] T. A. Costi, A. C. Hewson and V. Zlatic. *Transport coefficients of the Anderson model via the numerical renormalization group.* J. Phys. C **6**, 2519-2558 (1994)

[16] F. D. M. Haldane. *Scaling theory of the asymmetric Anderson model.* Phys. Rev. Lett. **40**, 416-419 (1978).

[17] *A poor man's derivation of scaling laws for the Kondo problem.* J. Phys. C: Solid State Phys. **3**, 2436-2441 (1970)

[18] J. R. Schrieffer and P. A. Wolff. *Relation between the Anderson and Kondo Hamiltonians.* Phys. Rev. **149**, 491-492 (1966).

[19] R. Helmes *Diploma thesis, The effect of Kondo correlations on the absorption spectrum of semiconductor quantum dots.* Fakultät für Physik der Ludwig-Maximilians-Universität München (2004)

[20] H. R. Krishna-murthy, J. W. Wilkins, and K. G. Wilson. *Renormalization-group approach to the Anderson model of dilute magnetic alloys. I. Static properties for the symmetric case.* Phys. Rev. B **21**, 1003-1043 (1980).

[21] R. Bulla, T. A. Costi and T. Pruschke. *Numerical renormalization group method for quantum impurity systems.* Rev. Mod. Phys. **80**, 395-450 (2008).

[22] F. B. Anders and A. Schiller. *Real-time dynamics in quantum-impurity systems: a time-dependent numerical renormalization group approach.* Phys. Rev. Lett. **95**, 196801 (2005).

[23] R. Peters, T. Pruschke and Frithjof B. Anders. *Numerical renormalization group approach to Green's functions for quantum impurity models.* Phys. Rev. B **74**, 245114 (2006)

[24] A. Weichselbaum and J. von Delft. *Sum-rule Conserving Spectral Functions from the Numerical Renormalization Group.* Phys. Rev. Lett. **99**, 076402 (2007).

[25] T. Hecht *PhD thesis, Numerical Renormalization Group studies of Correlation effects in Phase Coherent Transport through Quantum Dots.* Fakultät für Physik der Ludwig-Maximilians-Universität München (2008)

[26] G. D. Mahan. *Excitons in metals: infinite hole mass.* Phys. Rev., **163**, 612-617 (1967).

[27] P. Nozières and C. T. De Dominicis. *Singularities in the X-ray absorption and emission of metals. III. one-body theory exact solution.* Phys. Rev., **178**, 1097-1107 (1969).

[28] N. d'Ambrumenil, B. Muzykantskii. *Fermi gas response to time-dependent perturbations.* Phys. Rev. B **71**, 045326 (2005).

[29] J. J. Hopfield, *Comments on Sol. St. Phys.* **II**, 2 (1969).

[30] I. Affleck and A. Ludwig. *The Fermi-edge singularity and boundary condition changing operators.* J. Phys. A: Math. Gen. **27**, 5375-5392 (1994).

[31] P. W. Anderson. *Infrared catastrophe in fermi gases with local scattering potentials.* Phys. Rev. Lett. **18**, 1049-1051 (1967).

[32] R. W. Helmes, M. Sindel, L. Borda, and J. von Delft. *Absorption and emission in quantum dots: Fermi surface effects of Anderson excitons.* Phys. Rev. B **72**, 125301 (2005).

[33] H. Ishii. *Magnetic-field dependence of the bound state due to the s-d exchange interaction.* Progress of Theoretical Physics **40**, 201-109 (1968).

[34] P. Nozières. *"Fermi-liquid" description of the Kondo problem at low temperatures.* J. Low Temp. Phys. **17**, 31-42 (1974).

[35] J. Friedel. *On some electrical and magnetic properties of metallic solid solutions.* Can. J. Phys. **34**, 1190 (1956).

[36] D. C. Langreth. *Friedel sum rule for Anderson's model of localized impurity states.* Phys. Rev. **150**, 516 (1966).

Acknowledgement

I want to thank all people who were in some way involved in this thesis.

Prof. Dr. Jan von Delft for his advice and encouragement and showing me how to make a good presentation, scientific article, poster and meaningful figures.

Prof. Dr. Hakan Türeci for the exciting collaboration which turned out to be very fruitful.

Prof. Dr. Jonathan Finley for being the supervisor of this thesis and taking care it went to the right direction.

Dr. Theresa Hecht for introducing me into the NRG method and making the start of the Diploma thesis a lot easier.

Dr. Andreas Weichselbaum for making his highly efficient NRG code available to me and for his very competent advice with his vast knowledge about computer programming.

My roommates Wolfgang Münder, Arne Alex and Dr. Ireneusz Weymann for discussions about physics, life and everything and for a lot of "Berliners" for free.

All other people from the chair for the friendly working climate and the physical discussions.

The team of the Rbg with Ralph Simmler for keeping the fast and silent computers running.

My family for their support during the last year.

My friends for always rising my motivation.